ABSTRACT

Title of Dissertation: THE EFFECTS OF GRAVITY ON FLOW BOILING HEAT TRANSFER

Caleb Franklin Hammer,
Doctor of Philosophy, 2021

Dissertation directed by: Professor Jungho Kim
Department of Mechanical Engineering

Flow boiling is a method of phase change heat transfer used widely in electronics cooling, refrigeration, air conditioning, and other areas where stable temperatures are needed. An area of interest is spaceflight systems, where efficient heat transfer is desired to minimize mass, power requirements, and cost. When compared to terrestrial gravity conditions, the heat transfer of flow boiling in microgravity typically depreciates. This depreciation has been documented across multiple experimental studies performed by teams using different fluids, tube geometries, and flow regimes over the past three decades. Though select experimental microgravity flow boiling heat transfer data are available in the literature, holistic results are sparse due to the cost and limited availability of microgravity research. The two-phase heat transfer mechanisms responsible for the depreciation are therefore not well known, and so heat transfer models for variable gravity flow boiling do not exist.

The goal of the proposed study is to develop models for flow boiling heat transfer through a tube as a function of gravity by identifying the effect of gravity on different heat transfer mechanisms. The scope of this proposal involves modeling three microgravity flow regimes (bubbly, slug, and annular flow) to serve as baseline predictions for flow boiling heat transfer without the influence of gravity. Additional gravity effects can be identified using partial and hyper-gravity data.

Experiments have been performed aboard parabolic flights and on the ground at various flow rates, heating rates, and inlet subcoolings in microgravity, hyper-gravity, Lunar gravity, Martian gravity, and terrestrial gravity. Results from the experiments showed that negligible slip velocity plays an important role in modeling flow boiling heat transfer. Simulations using modified single-phase models of an accelerating flow were performed which predicted microgravity flow boiling heat transfer well in the nucleate boiling regime.

Additional experiments concerning terrestrial gravity quenching heat transfer have been performed to address research gaps in microgravity cryogen chilldown studies. Quenching heat transfer coefficients were recorded in the nucleate boiling regime and compared with correlations. The correlations were able to predict heat transfer for room temperature fluids much more accurately than for cryogenic fluids. Scaling parameters must be tuned to match cryogen data to examine the large disparity between cryogenic quenching heat transfer data and correlations observed in the literature.

THE EFFECTS OF GRAVITY ON FLOW BOILING HEAT TRANSFER

by

Caleb Franklin Hammer

Dissertation submitted to the Faculty of the Graduate School of the
University of Maryland, College Park in partial fulfillment
of the requirements for the degree of
Doctor of Philosophy
2021

Advisory Committee:

Professor Jungho Kim, Chair
Professor Christopher Cadou, Dean's Representative
Professor Kenneth Kiger
Professor Reinhard Radermacher
Professor Amir Riaz

ACKNOWLEDGEMENTS

My academic journey has given me the privilege of working with many inspiring people. The most valuable lesson I learned throughout my years at the University of Maryland is that the desire for knowledge and understanding is most contagious when surrounded by people who are truly passionate about their work. Professor Jungho Kim has been, without a doubt, the principal example in this regard. Being able to work alongside him and witness his devotion and near unquenchable thirst for discovery has been a source of inspiration that will continue to motivate me throughout my career. For that, I cannot thank him enough. I also had the pleasure of working with incredible peers who embodied this passion too. Michel, Cathleen, Catherine, Julien, Yutaku, Alex, and Valentin were each helpful and inspiring to me as both companions and fellow researchers.

The support I received from NASA played an integral part in my growth as a research scientist. To have been a recipient of the NASA Space Technology Research Fellowship is an honor that I proudly carry with me. The opportunity to work at NASA Glenn Research Center broadened my comprehension of the state-of-the-art and honed my capabilities as an engineer. I would like to thank John, Nancy, Marit, Tyler, and Luke for being not only being competent mentors, but also friends who showed joy and camaraderie in their passion for science.

Undoubtedly, the most support I received came from my family. The household I grew up in treated education and coursework in the highest regard. Through no part of my upbringing did this principle waver, and my family spared no effort in helping me along the way. My mother and father, Bette and Ed, always imparted more than enough valuable aid and encouragement. I would not have accomplished nearly as much as I have without

their unconditional love. My aunt, Kelly, who had the pleasure of obtaining her doctorate in education alongside my own pursuits, showed nothing but love, support, an ear to lend and a shoulder to lean on. My brother and sister, Curtis and Katie, however far away in the world they may be, never truly left my side throughout all my endeavors. Finally, I know my grandparents would be beyond proud of this accomplishment.

TABLE OF CONTENTS

LIST OF TABLES

LIST OF FIGURES

NOMENCLATURE

General

Symbol	Definition	Units
A	cross-sectional area	[m^2]
C_D	drag coefficient	[-]
C_P	specific heat capacity	[J/kg.K]
D	tube diameter	[m]
F_k	Kandlikar fluid constant	[-]
f_i	friction factor	[-]
G	mass flux	[$kg/m^2.s$]
h	heat transfer coefficient	[$W/m^2.K$]
h_{fg}	latent heat	[kJ/kg]
I	LED excitation intensity	[bits]
j	superficial velocity	[m/s]
k	thermal conductivity	[W/m.K]
l	tube length	[m]
$\dot{m}$	mass flux	[kg/s]
n	eddy diffusivity constant	[-]
P	pressure	[Pa]
p	perimeter	[m]
q”	heat flux	[W/m^2]
R	resistance	[Ω]
r	tube radius	[m]
T	temperature	[°C]
t	time	[s]
u	mean velocity	[m/s]
V	volume	[m^3]
v	velocity	[m/s]
x	vapor quality	[-]
X_{tt}	Martinelli parameter	[-]
z	axial distance from tube inlet	[mm]

Greek

Symbol	Definition	Units
α	thermal diffusivity	[m^2/s]
ΔT	temperature difference	[°C]
δ	film thickness	[m]
ε	eddy diffusivity	[m^2/s]
λ	wavelength	[m]
μ	dynamic viscosity	[Pa.s]
ν	kinematic viscosity	[m^2/s]
ρ	density	[kg/m^3]
σ	surface tension	[N/m]
τ	time constant	[s]
τ_i	interfacial shear stress	[Pa]

Subscripts

Symbol	Definition
B	buoyancy
b	bulk
bo	boiling
bu	bubble
C	critical
cb	convective boiling
D	drag
exp	experimental
F	forced
f	fluid
H	heated
i	inner
in	inlet
l	liquid
lam	laminar
m	mean
max	maximum
N	natural
NB	nucleate boiling
num	numerical
Q	constant heat flux
sat	saturation
sub	subcooled
t	terminal
T	constant temperature
v	vapor
w	wetted
+	positive error
-	negative error

Dimensionless Groups

Symbol	Name	Relationship	Definition
Bo	Boiling Number	$\frac{mass\ flux\ of\ vapor\ generation}{mass\ flux\ of\ bulk\ flow}$	$Bo = \frac{q''}{Gh_{fg}}$
Ja	Jakob Number	$\frac{sensible\ heat\ transfer}{latent\ heat\ transfer}$	$Ja = \frac{C_P(T_{sat} - T)}{k}$
Nu	Nusselt Number	$\frac{convective\ heat\ transfer}{conductive\ heat\ transfer}$	$Nu = \frac{hL}{k}$
Pr	Prandtl Number	$\frac{momentum\ diffusivity}{thermal\ diffusivity}$	$Pr = \frac{\mu C_P}{k}$
Re	Reynolds Number	$\frac{convective\ momentum\ transport}{viscous\ momentum\ transport}$	$Re = \frac{GD}{\mu}$
We	Weber Number	$\frac{inertial\ force}{surface\ tension\ force}$	$We = \frac{GD}{\rho\sigma}$

Acronyms

Symbol	Definition
CHF	critical heat flux
CNB	carbon nanobud
ID	inner diameter
IR	infrared
ITO	indium tin oxide
LED	light-emitting diode
LN_2	liquid nitrogen
NASA	National Aeronautics and Space Administration
PET	polyethylene terephthalate
PSP	pressure sensitive paint
TSP	temperature sensitive paint
UV	ultraviolet

CHAPTER 1: INTRODUCTION

1.1 BACKGROUND

1.1.1 Motivation

Flow boiling is a method of phase change heat transfer used widely in electronics cooling, refrigeration, air conditioning, and other areas where stable temperatures are needed. An area of interest is spaceflight systems, where efficient heat transfer is desired to minimize mass, power requirements, and cost. Two NASA workshops [1, 2] and two NRC reports [3, 4] highlighted thermal management (and phase change heat transfer in particular) for advanced life support and propulsion as one of the technologies critical for successful deployment of long duration missions. Most existing spacecraft thermal subsystems rely on single-phase heat transfer, but the drive towards lighter, smaller, higher power subsystems to make future missions possible will require use of two-phase thermal systems. The key challenge in developing two-phase thermal systems is the development of a heat transfer database and reliable models for flow boiling in variable gravity environments from which the performance of two-phase heat exchangers in spacecraft can be predicted confidently. The use of two-phase thermal systems on spacecraft has been greatly hampered by the inability to predict with sufficient confidence their performance at various gravity levels (Earth, Mars, and lunar gravity and low-g). The performance prediction of two-phase systems under these conditions requires a sufficient heat transfer database and reliable models, both of which are not currently available.

1.1.2 Microgravity Research

Past research using parabolic aircraft has resulted in better understanding of how flow boiling is altered in microgravity for a variety of test section geometries, working fluids, and flow regimes. Ohta [5] observed heat transfer deterioration in microgravity for R113 annular flow through an 8 mm ID tube using a heated thin gold film on the inner wall to obtain average temperature values. He suggested the deterioration was due to the larger thickness and lower frequency of passing liquid troughs in the thin film that were observed in microgravity. Heat transfer became gravity independent at a mass flow of 600 kg/(m^2.s). Baltis et al. [6] measured heat transfer of FC-72 along a horizontal tube using thermocouples along the outer wall of 2 mm ID, 4 mm ID, and 6 mm ID tubes. Heat transfer and bubble size became independent of gravity level above a mass flux of 425 kg/(m^2.s) for their 6 mm ID tube. For their 4 mm ID tube, a maximum difference of ±8% was observed between microgravity and terrestrial gravity heat transfer coefficients. Significant flow instabilities and thermal crises were observed for their 2 mm ID tube at low gravity, making direct comparisons for tube diameter non-trivial. They also reported heat transfer enhancement for conditions where the microgravity flow was intermittent and terrestrial flow was bubbly. Narcy et al. [7] studied microgravity flow boiling for HFE-7000 in a 6 mm ID sapphire tube heated by a transparent ITO layer on the outside. At low mass flow rate in microgravity, the bubbles sizes were larger than in 1-g upward flow and the heat transfer was lower. For mass fluxes greater than 540 kg/(m^2.s), little difference in bubble size and shape were observed. The heat transfer became independent of gravity for mass fluxes greater than 200 kg/(m^2.s). The differences in mass flux limits among the researcher

can perhaps be attributed to variations in the researchers' test tube dimensions, working fluids, and heat flux ranges.

Critical heat flux (CHF) in flow boiling can occur by applying a large wall heat flux to a short tube, thereby raising the wall temperature sufficiently to vaporize the near-wall liquid and "lifting off" the fluid from wall (reverse annular flow). Zhang et al. [8, 9] developed a model that assumes CHF occurs when the wetting fronts of a wavy interface that periodically rewet a heated wall lift off due to vapor produced at the wall. Zhang et al. [10] used a 101.6 mm long rectangular channel with a single heated wall using FC-72 to validate their model. They performed experiments on parabolic aircraft with mass fluxes between 230 - 2500 kg/(m^2.s) and heat fluxes up to 28.4 W/cm^2. When CHF occurred in the channel, a wavy vapor layer almost fully separated the bulk liquid flow from the heated wall. The wavy vapor layer became superheated while the liquid remained subcooled at the outlet, resulting in little change in quality in the flow direction. They found the difference between CHF in microgravity and horizontal 1-g flow decreased with increasing mass flux, and the CHF performance converged at a mass flux of 2500 kg/(m^2.s).

CHF can also occur by applying a small wall heat flux along a sufficiently long channel during which various flow regimes such as bubbly, slug, slug-annular, and annular flow are often observed. CHF is thought to occur due to dryout or breakdown of the thin film in the annular region. There have been no studies of data regarding gravity effects on CHF during low heat flux heating. This dearth of data is likely due to the difficulty of designing a test apparatus that has sufficiently long heated length since space and/or power can be limited on microgravity platforms (drop towers, parabolic aircraft, sounding rockets, and other space-based systems).

1.1.3 Local Measurement Techniques

Definitive understanding of phase change heat transfer mechanisms even in terrestrial gravity remains elusive due to a lack of reliable local information for model testing and evaluation. If the heat transfer distribution along the walls of a tube could be measured, heat transfer models for slug flow, wavy annular flow, annular flow dryout, etc. could be verified. Low-cost techniques to measure local heat transfer coefficient distributions are thus needed.

Optical methods of temperature measurement have significant advantages over thermocouples, resistance thermometers, microheater arrays, and other techniques when access to the surface is available in the wavelength used. These include the ability to quantitatively measure temperature distributions over large areas non-invasively, at high speeds, over large temperature range, from long distances, and without exposing the measuring instrument to harsh environments if measurements can be made through a window. The most commonly used optical technique to measure wall heat transfer distributions during phase change has been based on infrared (IR) thermometry. IR thermometry has been used in the past [11], but there are drawbacks to this technique. The test section must be made of an IR-transparent, high thermal conductivity material such as silicon, which restricts visual access since it is opaque at visual wavelengths. The process of isolating the inner wall temperature using IR thermometry involves accounting for the effects of self-emission of the tube and reflection from the surroundings. This process can be computationally expensive depending on the tube wall construction and accurate values of the optical properties of the tube materials are needed.

1.1.4 Temperature Sensitive Paints

There is a strong need for a low-cost, optical measurement technique by which local heat transfer coefficients can be measured. Fluorescent paints that are sensitive to oxygen concentration (pressure sensitive paints, PSP) and temperature (TSP) have been used to measure shear stress, surface pressure, and wall temperature distributions in aerodynamic applications since the 1980s [12,13]. To measure temperature alone, the sensitivity to oxygen can be eliminated by encapsulation or removal of oxygen from the system. The paints are typically excited by blue/UV light and fluoresce at a longer wavelength. As temperature increases, the intensity of the emitted light decreases and the peak in the spectrum shifts to longer wavelengths. TSP calibration can be performed in-situ which eliminates intensity variation due to concentration. Kim and Yoda [14] developed a technique to measure fluid temperature within 100 nm of a wall using evanescent waves to illuminate a fluorescing tracer within the bulk fluid in single-phase flow, but this method becomes difficult to apply to two-phase flows since the local dye concentration can fluctuate due to evaporation. Shibuya et al. [15] applied TSPs to measure time varying two-phase flow heat transfer in a microgap. Al Hashimi et al. [16] demonstrated a TSP technique to measure time resolved wall temperature and heat transfer distributions during pool and flow boiling. A film of fluorescing paint was laminated directly onto a surface of interest, and they were able to document the unique wall heat transfer signatures during pool boiling, and single phase and two-phase flows in tubes.

1.2 OBJECTIVES

The goal of this study is to refine models for flow boiling heat transfer through a tube by identifying the significant effects of gravity on different heat transfer mechanisms. The

scope involves analyzing heat transfer in three microgravity flow regimes (bubbly, slug, and annular flow) at various flow conditions to serve as baseline predictions for flow boiling heat transfer without the influence of gravity. Insights into the dominance of certain mechanisms, such as surface tension and buoyancy described in Raj and Kim [17], will help determine the modeling considerations for flow boiling as a function of gravity. The effects of gravity on flow boiling are identified using experimental local heat transfer coefficient results published in Lebon et al. [18] obtained for terrestrial gravity, hyper gravity (1.8g), microgravity, and partial gravity (Lunar and Martian). Simulations published in Lebon et al. [19] are used to verify the conclusions made for microgravity bubbly flow boiling.

Additional ground data are taken in the form of quenching tests to begin comparing modeling results to microgravity cryogen chilldown experiments. Conventional models for flow boiling heat transfer coefficient significantly overpredict experimental cryogen transfer line quenching data, even in terrestrial gravity [20]. Transient effects involved in the chilldown process are not captured by models made for steady state heated tubes. Quenching data using a room temperature engineering fluid were recorded in the nucleate boiling regime for two cooling conditions to analyze transient effects. Comparisons are made between cryogen heat transfer and room temperature fluid heat transfer during the chilldown process. The application of findings made in modeling microgravity flow boiling heat transfer will provide insight for future quenching experiments.

CHAPTER 2: EXPERIMENT DESCRIPTION

2.1 TEST SECTION AND FLOW LOOP

The TSP-based test section and data reduction process developed and published by Al Hashimi et al. [16] were used to acquire preliminary data for this proposal. Heat flux and temperature as well as flow visualization were measured in the test section shown in Figure 2.1. The fluid flowed through a 6 mm ID/8 mm OD, 120 mm long sapphire tube. The tube is recessed 2.5 mm into Hydlar-Z endcaps on either end and sealed using O-rings. A PET (polyethylene terephthalate) film coated with a transparent Carbon NanoBud conductive layer (Canatu CNB Flex Film, 100 Ω/sq) was attached to the outside of the sapphire tube so it could be resistively heated. Silver paint was used to make electrical connections to copper electrodes on either end of the heaters. Roughly 5 mm of heat shrink was used to insulate each electrical connection, allowing 105 mm of the sapphire tube to be visualized. One half of the inside surface was covered with a PET 3M tape (3M 8911) onto which TSP and an opaque NiCr layer were attached so wall temperature could be measured. The other half of the tube was covered using the same 3M tape but without the TSP/NiCr to allow flow visualization. The opaque layer was included to block the excitation light from reflecting off bubbles within the flow and changing the TSP illumination intensity. Access to opposite sides of the tube allows the acquisition of temporally and spatially synchronized wall temperature and flow visualization videos, enabling direct correlation of flow/bubble phenomena with temperature fluctuations. The TSP was encapsulated between two layers of 5 micron thick adhesive (3M 82600) to protect it. A submicron thick, opaque germanium layer was deposited using an electron beam evaporator onto the adhesive side of the tape in a 1 mm diameter dot pattern at 10 mm spacing. TSP was painted onto the dots and used

to measure the temperature at the 3M tape/sapphire interface. The temperature profile at the tape-sapphire interface could be interpolated from the dot temperature values spaced 10 mm apart due to the high thermal conductivity of the sapphire. The temperature gradient between dots never exceeded 0.05°C/mm, while the minimum temperature gradient at the wall-fluid interface was ~5°C/mm. Measured properties of the acrylic adhesive are summarized in Table 2.1.

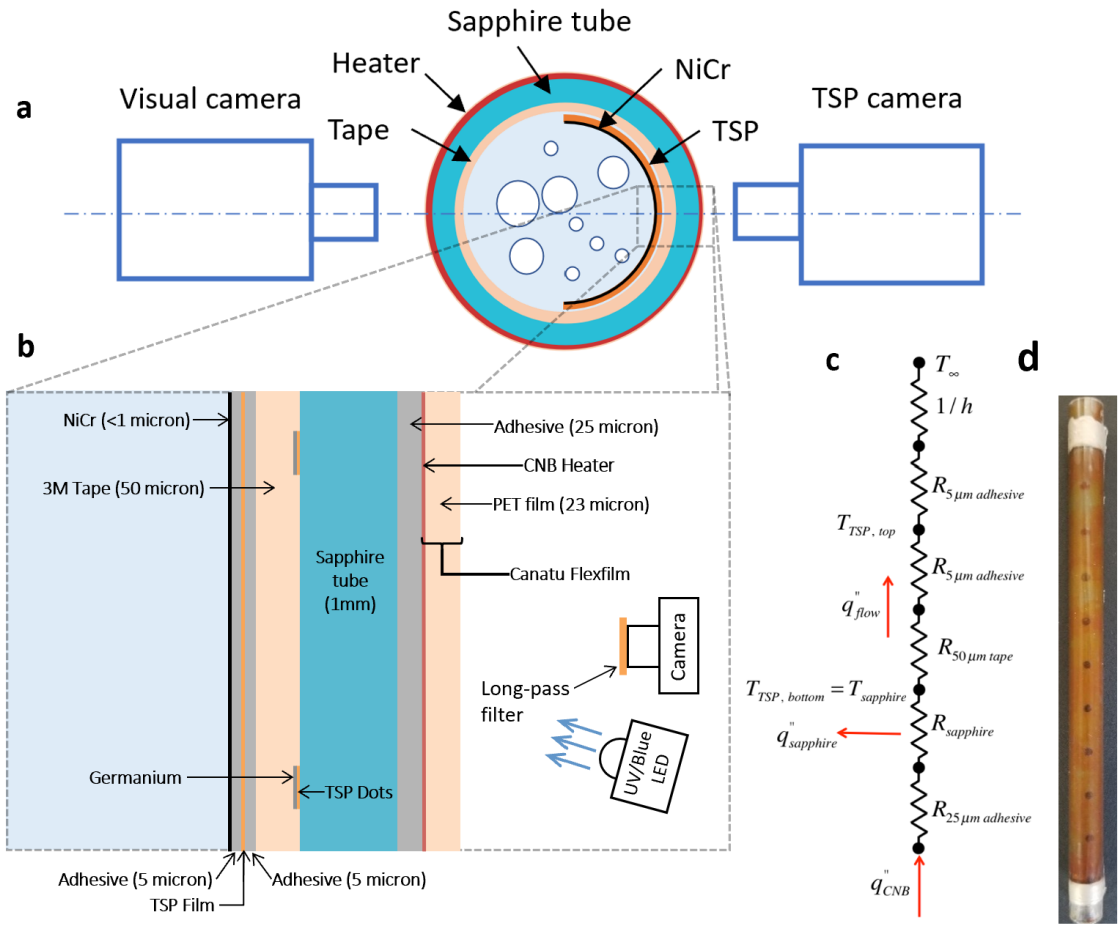

Figure 2.1: Test section diagrams including a) schematic of the tube cross section (not to scale), b) schematic of flow boiling heat transfer measurement stack (not to scale), c) thermal circuit used for determining heat transfer, and d) fully assembled sapphire tube.

Table 2.1: Acrylic adhesive and sapphire properties.

		Adhesive	**Sapphire (25°C)**
k	Thermal Conductivity (W/m.K)	0.21	25
C_p	Specific Heat (J/kg.K)	1800	780
ρ	Density (kg/m^3)	1180	3980

A high-speed camera (Phantom Miro eX4) was used to measure the TSP intensity and a second high-speed camera (Sentech STC-MBCM200U3V) was used for flow visualization. The 12-bit TSP videos were recorded for 1.6 s at 300 Hz or 3.2 s at 150 Hz while the 8-bit flow visualization videos were taken over 20 s at a frame rate of 600 Hz. Both cameras captured the triggering of the UV excitation light which was used to synchronize the videos during post-processing.

The flow loop is shown schematically in Figure 2.2 and the properties of the working fluid (3M Novec HFE-7000) are given in Table 2.2. Additional properties were interpolated from Rausch et al. [21]. A four-way valve in the loop enabled the flow to be quickly reversed, enabling data to be obtained during upward and downward flow when operating in a gravity field. A straight, unheated 6 mm ID copper tube 330 mm in length before the heated section resulted in hydrodynamically fully developed and thermally developing flows for Re<1100 and developing thermal and hydrodynamic for 1100<Re<2300. The copper tube is insulated and mates to the endcap holding the sapphire tube through a 6 mm ID orifice. The TSP technique and test section was validated in these regimes using single-phase flow experiments as described in Al Hashimi et al. [16].

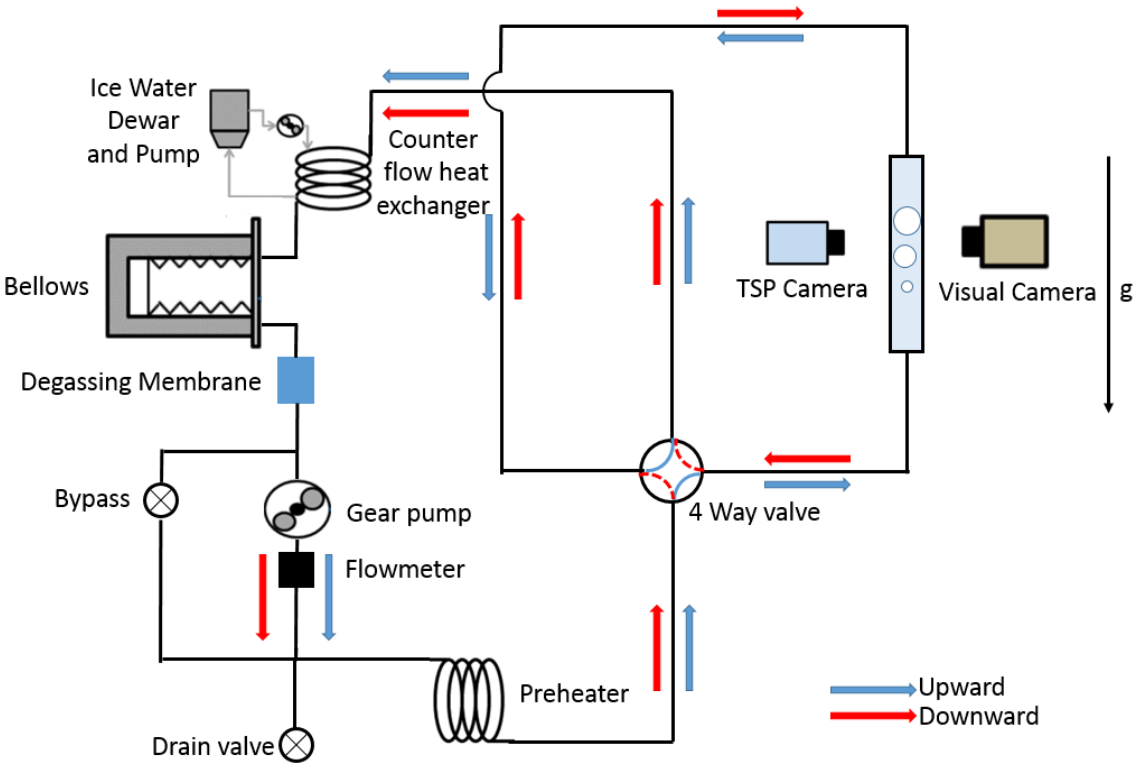

Figure 2.2: Flow boiling test loop.

Table 2.2: HFE-7000 properties at 25°C.

Parameter	**Value**
Density (kg/m^3)	1400
Thermal conductivity (W/m.K)	0.075
Kinematic Viscosity (m^2/s)	3.2×10^{-7}
Specific Heat (J/kg.K)	1300
Surface Tension (N/m)	0.0124
Latent Heat of Vaporization (kJ/kg)	142

The spectral characteristics of the TSP, the LED used for excitation, and the long-pass filter are shown in Figure 2.3. UV LEDs (3-Up SemiLED UV, 400-410 nm) were used to excite the TSP and a long-pass filter with a cutoff wavelength of 532 nm was used to isolate the TSP emission. The emission lifetime of the TSP used in this study, dichlorotris

(1,10-phenanthroline) ruthenium (II) hydrate, was on the order of microseconds, so the system frequency response was limited by the thermal response of the materials onto which the paint was bonded. The TSP had a high sensitivity, was inexpensive (~$100/g from Sigma Aldrich), and had a useful temperature range of 0-147°C. The temperature resolution was approximately -80 bits/°C using the 12-bit Phantom Miro eX4 even at the highest temperature in the experiment (~55°C), indicating accurate steady state measurements could be obtained by time averaging.

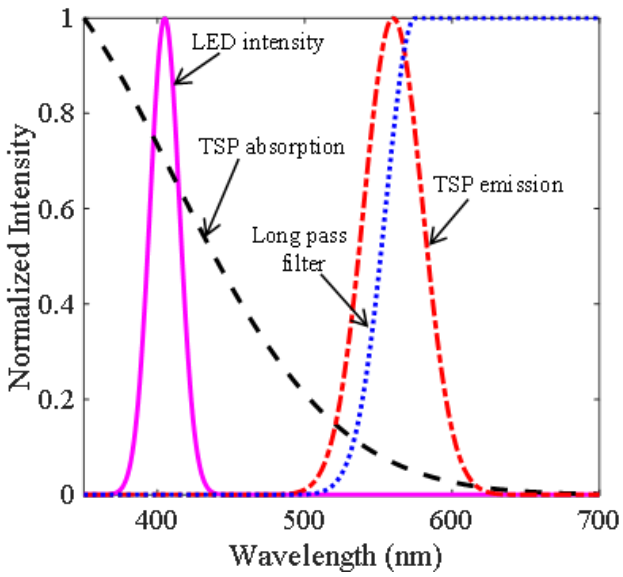

Figure 2.3: Spectral characteristics of TSP excitation and emission.

A photomultiplier (Hamamatsu R3788) was used to monitor and correct for any variations in UV light intensity, and the UV was only turned on for 3 s during each run to minimize TSP emission decay due to photobleaching. The Phantom camera exposure time was kept constant to eliminate automatic intensity correction. Green LEDs (3-Up Cree XPG2) were used to illuminate the visual side of the tube of the test section so any light leaking through the NiCr layer would not excite the TSP layer and cause extraneous

emission. The long-pass filter could effectively remove any light that did leak through. The measured temperature was independent of whether or not the green LEDs were powered.

In situ calibration of the TSP at each pixel was performed by pressurizing the flow loop to 2.4 bar (T_{sat}=62°C) to prevent boiling and pumping liquid at the desired temperature through the unheated test section. The flow rate was set at the maximum flow rate of 300 mL/min to minimize the temperature drop along the test section. The test section inlet and outlet temperatures were measured using thermocouples inserted into the flow. TSP intensity distributions were recorded for liquid temperatures between 25°C and 60°C in increments of 5°C. 2nd order polynomials were fit to the intensity vs. temperature data at each pixel. The calibration for a representative pixel at three UV-LED intensities is shown in Figure 2.4.

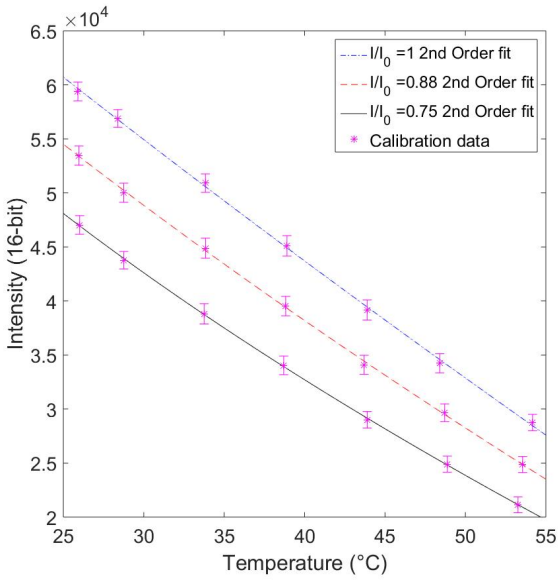

Figure 2.4: TSP calibration for a representative pixel at three UV-LED intensities.

A schematic of the heat flow within the test section is shown in Fig. 2.2. Heat was added to the outside of the tube by the CNB heater ($\dot{q}''_{CNB}$). Part of this heat flows axially along the sapphire tube ($\dot{q}''_{sapphire}$), while the remainder flows through the 50 micron 3M

tape and adhesive, and into the fluid ($\dot{q}''_{flow}$). Heat flux into the fluid was calculated using Fourier's Law:

$$\dot{q}'' = -k\frac{dT}{dx} \tag{1}$$

An unsteady heat conduction code was used to resolve the temperature distribution throughout the 3M tape using the TSP film and TSP dot temperatures as boundary conditions. The heat flux into the fluid was calculated using the time resolved temperature gradient at the TSP film and the properties of the 3M tape. The heat transfer coefficient at each pixel was calculated using the local heat transfer, the local wall temperature, and the bulk fluid temperature:

$$h = \frac{\dot{q}''_{flow}}{(T_{TSP} - T_{bulk})} \tag{2}$$

The bulk fluid temperature was calculated using an energy balance along the length of the tube:

$$T_{bulk} = \frac{2\int_0^z \dot{q}''(z)dz}{GC_P r_i} \tag{3}$$

Measurement uncertainty was dependent on the TSP calibration, physical properties, thermocouple errors, camera noise, and test section dimensions. The uncertainty in the unsteady wall heat flux was dominated by camera noise. For steady state heat transfer, spatial and temporal averaging of the temperature can be used to minimize errors due to camera noise. The uncertainties in wall heat flux for microgravity at G=40 kg/(m^2.s) are summarized in Table 2.3. Both steady and unsteady uncertainties remain relatively constant with heat flux, so the percentage uncertainty decreases as wall heat flux increases. For unsteady measurements, the uncertainty percentage decreased from 58% at 0.75 W/cm^2

to 18% at 1.85 W/cm^2. These trends are consistent at higher flow rates. The uncertainty bars at steady state conditions are indicated on all data points and vary between 0.05-0.15 W/cm^2 (5-12%).

Table 2.3: Heat flux uncertainty for G=40 kg/(m2.s) (95% confidence interval).

	0.75 W/cm^2			**1.85 W/cm^2**		
	-1g	μg	1g	-1g	μg	1g
Wall heat flux (W/cm^2)	0.57	0.32	0.64	1.82	1.70	1.87
Steady state uncertainty (W/cm^2)	0.06	0.05	0.05	0.12	0.08	0.15
Unsteady uncertainty (W/cm^2)	0.28	0.28	0.28	0.29	0.29	0.30

CHAPTER 3: EXPERIMENTAL RESULTS AND DISCUSSION

Experiments on microgravity subcooled flow boiling were performed as published in Lebon et al. [18]. Flow boiling results were acquired in upward flow, downward flow, and microgravity for nine gravity levels (-1.8, -1.0, -0.34, -0.16, 0, 0.18, 0.36, 1.0, and 1.8 g), six nominal heat fluxes (0.25, 0.5, 0.7, 1.0, 1.5, and 1.85 W/cm^2), and four mass fluxes (40, 60, 80, and 120 kg/(m^2.s)) at two subcoolings (~10°C and ~4°C). Microgravity (μg) measurements were obtained through a NASA funded program to fly the experiment on the Zero Gravity Corporation parabolic aircraft. Each parabola consisted of a ~30 s 1.8g pull-up, ~22 seconds of microgravity, and a ~30 s 1.8g pull-out. The airside of the accumulator was fixed at 1 atm to prevent fluctuations in aircraft cabin pressure from affecting the flow loop.

The heat transfer coefficient was averaged over the rectangular areas shown below in the respective figures for each data point, which was halfway along the heated length of the tube. The differences in plotted tube lengths were due to the presence of a thermocouple on the tube outer wall, which obscured different areas of the tube during different tests. Partial delamination of the TSP film sometimes occurred during testing at higher heat fluxes but did not affect the heat transfer over the measurement area. The heat flux values in the figures below (represented by different shapes and colors) are the average of the local heat flux between the inlet and midpoint of the tube. The difference between the nominal input heat flux from the CNB and the measured heat flux is attributed to tube end conduction, radiation to the ambient, and natural convection at the tube's outer wall.

3.1 EFFECT OF MASS FLUX AND HEAT FLUX

3.1.1 Upward Flow

During upward flow, the inertial and buoyancy forces on the bubble act in the same direction and aid bubble detachment from the wall against the capillary force (Lebon [22]). Bubbly flow with spherical bubbles was observed for most upward flow conditions. The heat transfer coefficients at the center of the tube for 1g flow are shown for two inlet subcoolings on Figure 3.1. The heat transfer coefficient typically increased with increasing mass flux and/or heat flux. At low heat fluxes and high mass fluxes, however, the increase in mass flux caused all nucleation sites to deactivate and single phase flow occurred along the entire length of the tube (these cases are marked "Single phase"), resulting in a lower heat transfer coefficient. For 10.1°C of subcooling, single phase flow was observed at heat fluxes of 0.52 W/cm^2 and 0.67 W/cm^2 (Figure 3.1 left). For the lower inlet subcooling of 3.9°C (Figure 3.1 right), single phase flow occurred only at a lower heat flux of 0.31 W/cm^2.

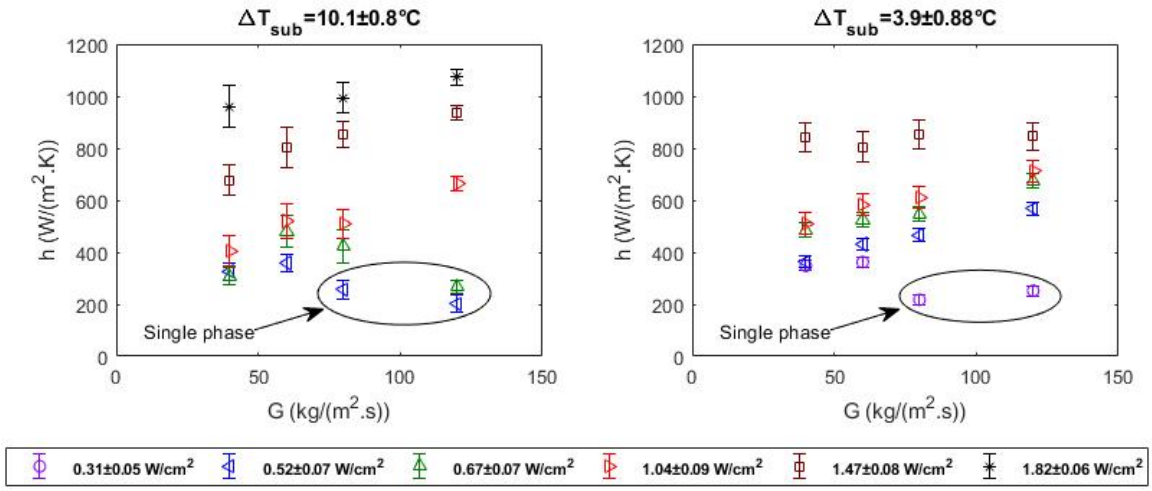

Figure 3.1: Upward flow: evolution of the heat transfer coefficient versus mass flux at various heat fluxes, 10.1°C of subcooling (left) and 3.9°C of subcooling (right).

The instantaneous heat transfer coefficient along a line of pixels for a heat flux of 1.04 W/cm^2 at three mass fluxes are shown Figure 3.2. The flow entered the bottom of the tube as subcooled liquid, and the heat transfer coefficient decreased as the thermal boundary layer developed. A jump in the heat transfer occurred due to two-phase turbulent mixing once nucleation was initiated (see arrows in Figure 3.2). The location at which nucleation initially occurred moved downstream as mass flux increased.

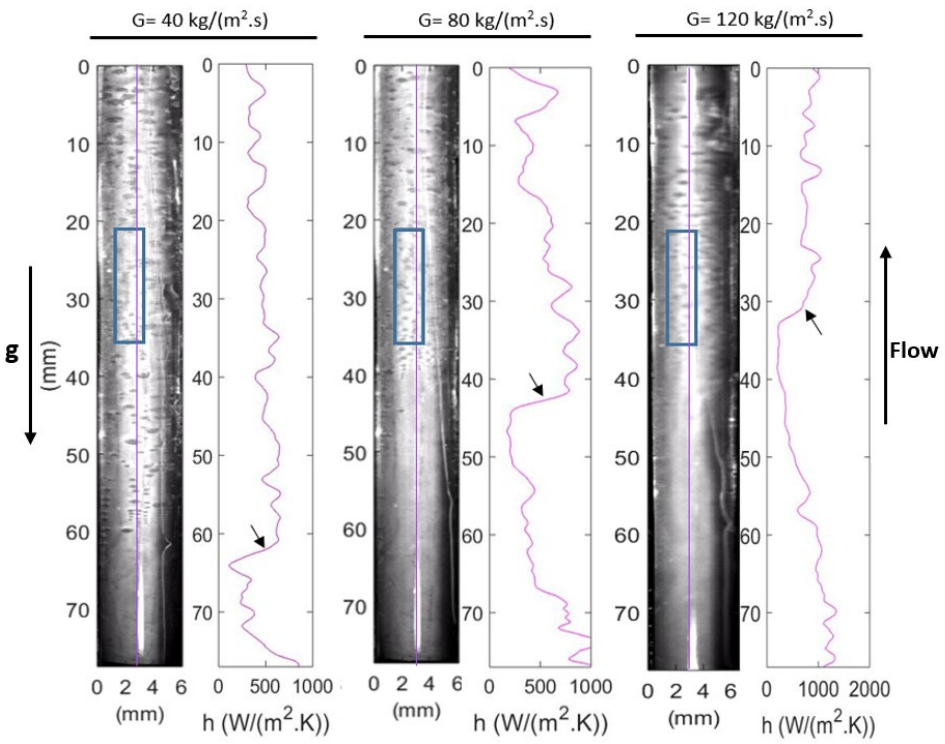

Figure 3.2: Upward flow: heat transfer coefficients for q"=1.04±0.09 W/cm^2.

For Re=1100, the entry length was 33 cm, which was similar to the length of straight tube (34 cm) upstream of the test section, so the flow below this Reynolds number was hydrodynamically fully developed. The measured heat transfer coefficients just before the first nucleation site were compared to the single-phase mixed convection correlation for single phase, upward flow ($Nu^n = Nu_F^n \pm Nu_N^n$) where n=3 for vertical cylinders [23]. The natural convection correlation for a vertical open tube by Davis and Perona [24] (equation 4) and the forced convection correlation by Shah & London. [25] (equations 5 and 6) were used. For Re>1100, the flow was hydrodynamically and thermally developing so the Davis and Perona [24] (equation 4) and Stephan [26] (equation 7) correlations were used. Figure 3.3 compares the experimental data with these single-phase correlations. The data are separated into Nusselt numbers observed for cases where single phase was

observed along the entire length of the tube and cases where nucleation was initiated at a point in the tube. The Nusselt numbers for the latter cases were taken at an area just upstream of the initial nucleation site. The data agree to within 15% with the values given by the correlations.

$$Nu_N = 0.61(Gr^* Pr)^{1/4}, Gr^* = \frac{g(T_w - T_m)r^4}{\bar{T}_m l \nu^2} \tag{4}$$

$$Nu_F = Nu_0 \left(\frac{\mu}{\mu_w}\right)^{0.14} \tag{5}$$

$$Nu_0 = \begin{cases} 1.953\left(RePr\dfrac{D}{l}\right)^{1/3}, & RePr\dfrac{D}{l} \geq 33.3 \\ 4.364 + 0.0722RePr\dfrac{D}{l}, & RePr\dfrac{D}{l} < 33.3 \end{cases} \tag{6}$$

$$Nu_F = 4.364 + \frac{0.086\left(RePr\frac{D}{l}\right)^{1.33}}{1 + 0.1\,\mathrm{Pr}\left(Re\frac{D}{l}\right)^{0.83}}, Pr > 7 \; or \; RePr\frac{D}{l} < 33.3 \tag{7}$$

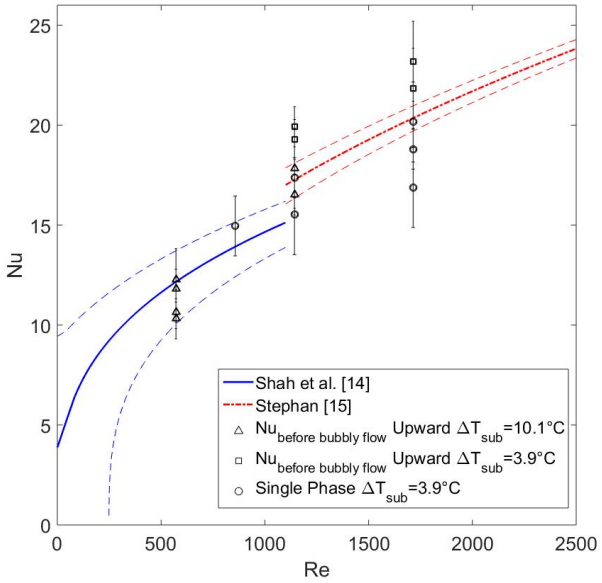

Figure 3.3: Upward flow: comparison of experimental and single-phase mixed convection correlations.

The effect of heat flux on the instantaneous heat transfer coefficient along the tube at G=40 kg/(m^2.s) is shown on Figure 3.4. The location at which nucleation occurred moved upstream as heat flux increased. The bubble size remained small throughout the tube even at higher heat fluxes. At the end of the tube for a heat flux of 1.82 W/cm^2, bubbles coalesced, and the heat transfer coefficient increased gradually as the flow began to transition from bubbly flow to annular flow.

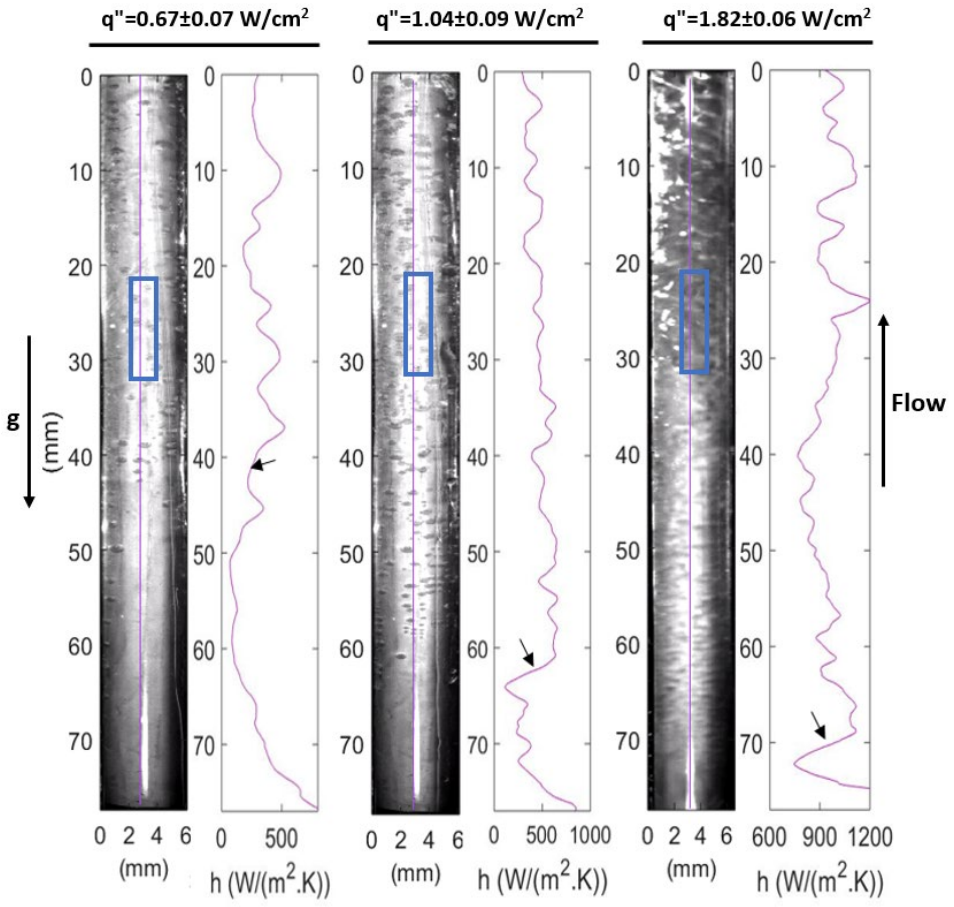

Figure 3.4: Upward flow: heat transfer coefficients for G=40 kg/(m^2.s).

3.1.2 Microgravity Flow

In microgravity, the slip velocity has been shown to be very small (Colin et al. [27]). Only inertial forces aid bubble detachment against capillary forces, allowing bubbles to grow much larger before detaching. The average heat transfer coefficient generally increased with mass flux and/or heat flux (Figure 3.5), which is the same trend observed for upward flow. No single-phase flow was observed for microgravity data at 9.7°C of subcooling. Two-phase flow was observed at lower heat fluxes than in upward flow. Due to the absence of natural convective cooling, the microgravity thermal boundary layer grew more quickly. The higher wall temperature promoted more nucleation within the tube. Single-phase flow

was only observed at 4.2°C of subcooling for G=120 kg/(m^2.s) and a heat flux of 0.34 W/cm^2.

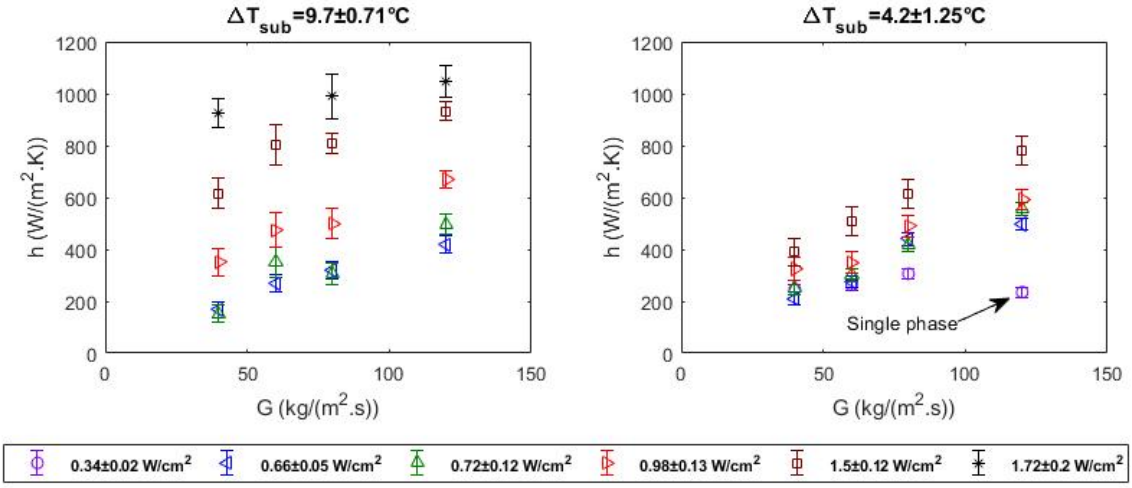

Figure 3.5: Microgravity: evolution of the heat transfer coefficient versus the mass flux at various heat fluxes for 10°C of subcooling (left) and 4°C of subcooling (right).

The instantaneous heat transfer coefficient along the tube for a heat flux of 0.98 W/cm^2 at three mass fluxes is shown in Figure 3.6. Bubbly flow with large spherical bubbles dominated the microgravity experiments. Bubbles coalesced frequently at low mass flux. Large capillary bubbles formed and rapidly expanded through the tube (e.g., G=40 kg/(m^2.s) at 30-45 mm in Figure 3.6) due to the frequent coalescence and the high temperature liquid film near the wall. The heat transfer coefficient increased at the inlet of the tube once nucleation occurred. As the mass flux increased, the bubble diameter at detachment decreased. At G=80 kg/(m^2.s), an increase in heat transfer coefficient was observed at the inlet as well as at 30 mm. It is possible that the introduction of more nucleation sites at this point could have caused a localized increase in heat transfer coefficient, though it is not clear in the visual frames if more sites were active. At G=120 kg/(m^2.s), an increase in heat transfer coefficient at the tube inlet occurred followed by a

gradual decrease. This decrease in heat transfer coefficient is due to larger size of the bubbles that may affect nucleation sites which can be covered or deactivated by larger bubbles.

The instantaneous heat transfer coefficients for G=40 kg/(m^2.s) at three heat fluxes are shown Figure 3.7. As the heat flux increased, bubble diameter at detachment increased and bubbles coalesced to form an annular flow at high heat flux (Figure 3.7 right). An increase in heat transfer coefficient was observed with increasing heat flux.

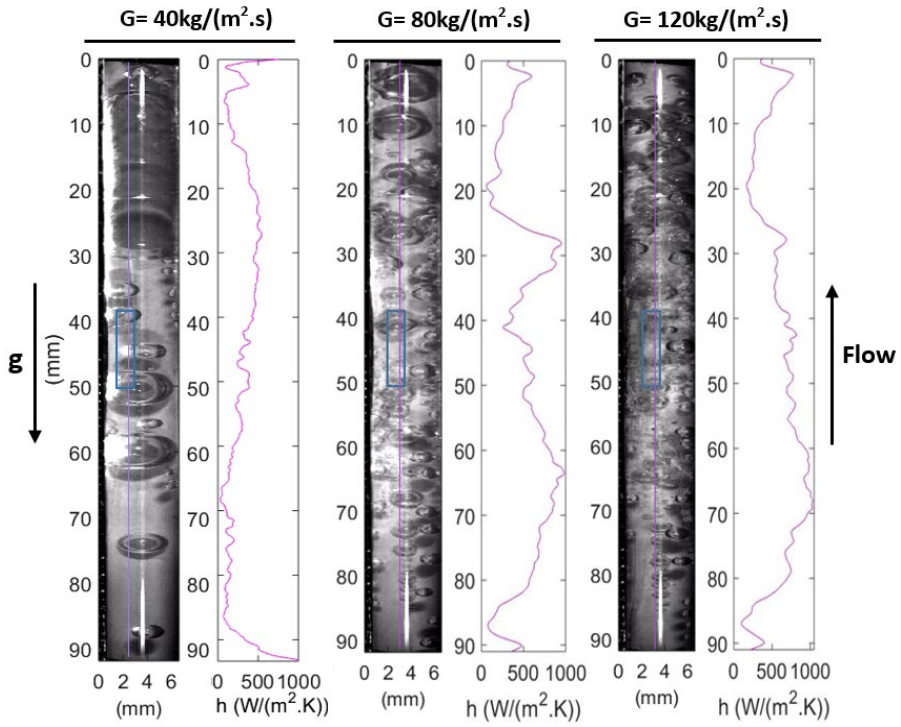

Figure 3.6: Microgravity: heat transfer coefficients for q"=0.98±0.13 W/cm^2.

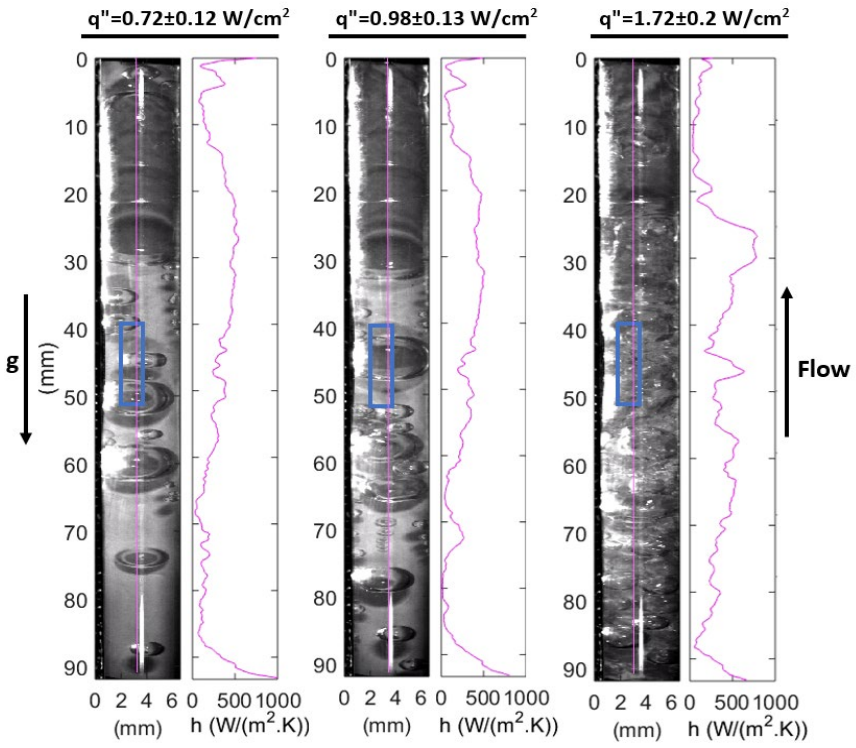

Figure 3.7: Microgravity: heat transfer coefficients for G=40 kg/(m^2.s).

3.1.3 Downward Flow

For downward flow, the buoyancy force on the bubble opposes the bulk fluid motion, creating a large slip velocity. Bubbly flow, stationary bubbles, churn flow, and falling film regimes were observed. Flat, elliptical bubbles were observed in bubbly flow. At lower mass fluxes, bubbles often travelled in the direction opposite to the bulk flow since the buoyancy force was greater than the hydrodynamic force. This created a significant flow instability which resulted in complex regime transition behavior. The evolution of the average heat transfer coefficient with increasing mass flux is shown on Figure 3.8. The heat transfer coefficient typically increased with mass flux and/or heat flux similar to upward flow and microgravity. Single-phase flow occurred along the entire length of the tube at 0.55 W/cm^2 for mass fluxes of 80 and 120 kg/(m^2.s) for 10.5°C subcooling and at

0.31 W/cm^2 for mass fluxes of 60, 80, and 120 kg/(m^2.s) for 4.4°C subcooling. The strong mixing caused by opposing natural and forced convection terms resulted in a high enough heat transfer to suppress nucleation in these cases. Increasing heat flux created more nucleation sites as bubbles coalesced into Taylor bubbles which slowly grew as they accelerated against the flow. The changing speed of the bubble in these cases caused churn flow to occur. At high heat flux, falling film was observed for each mass flux.

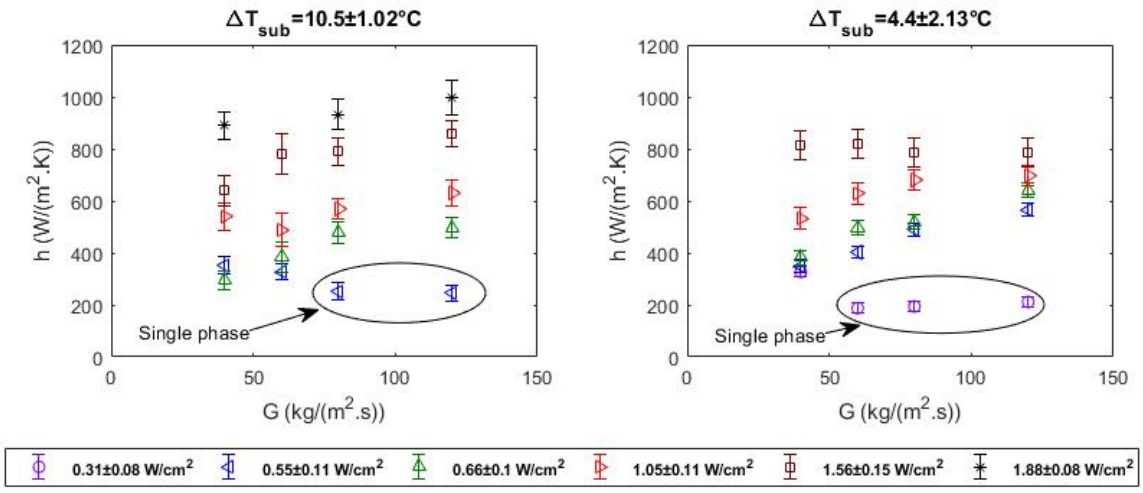

Figure 3.8: Downward flow: heat transfer coefficient vs. mass flux at various heat fluxes for 10.5°C subcooling (left) and 4.4°C subcooling (right).

Comparison of visual images and heat transfer coefficient at a heat flux of 1.05 W/cm^2 for three mass fluxes is shown in Figure 3.9. At G=40 kg/(m^2.s), bubbles occasionally merged to form a vapor slug which slowly grew as it moved upward (upstream) against the flow. The heat transfer decreased as the flow accelerated around the slug due to suppression of nucleation. The heat transfer coefficient steadily increased at the head and tail of the slugs (Figure 3.9 left). Increasing the mass flux to G=80 kg/(m^2.s) (Figure 3.9 center) resulted in smaller bubbles that moved more slowly upward against the flow. The heat transfer was highest towards the top of the tube where the bubble density

was largest. At G=120 kg/(m^2.s), a critical point was reached where the buoyancy force approximately matched the drag force which allowed the bubbles to coalesce into an oscillating Taylor bubble. A peak in heat flux was seen in the wake of the Taylor bubble. The high heat transfer ahead of the bubble is due to the presence of a nucleation site.

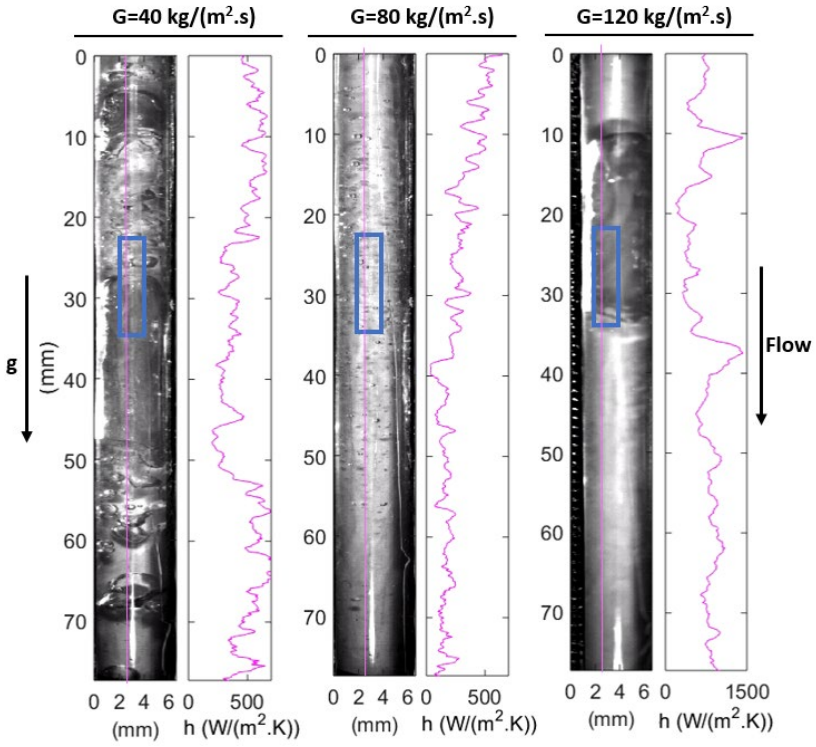

Figure 3.9: Downward flow: heat transfer coefficients for q"=1.05±0.11 W/cm^2.

The instantaneous heat transfer coefficient along a line of pixels for G=40 kg/(m^2.s) at three heat fluxes are shown Figure 3.10. The nucleation site density increased with heat flux. The flow regime changed from bubbly flow (0.66 W/cm^2) to bubbly flow with intermittent Taylor bubbles (1.05 W/cm^2) and finally to annular flow with a falling film (1.88 W/cm^2). In the bubbly flow regime, bubbles were larger towards the outlet of the tube and travelled in the direction opposite to the flow. An increase in heat transfer coefficient was observed at the outlet due to stronger mixing around the larger bubbles.

The Taylor bubbles moved upward intermittently, causing the heat transfer to oscillate with time—low heat transfer within the thin film and higher heat transfer on either end of the Taylor bubble–due to two-phase turbulent mixing (Scammell & Kim [28]). The heat transfer coefficient along the falling film was more consistent than the other stratified and intermittent flows observed in downward flow.

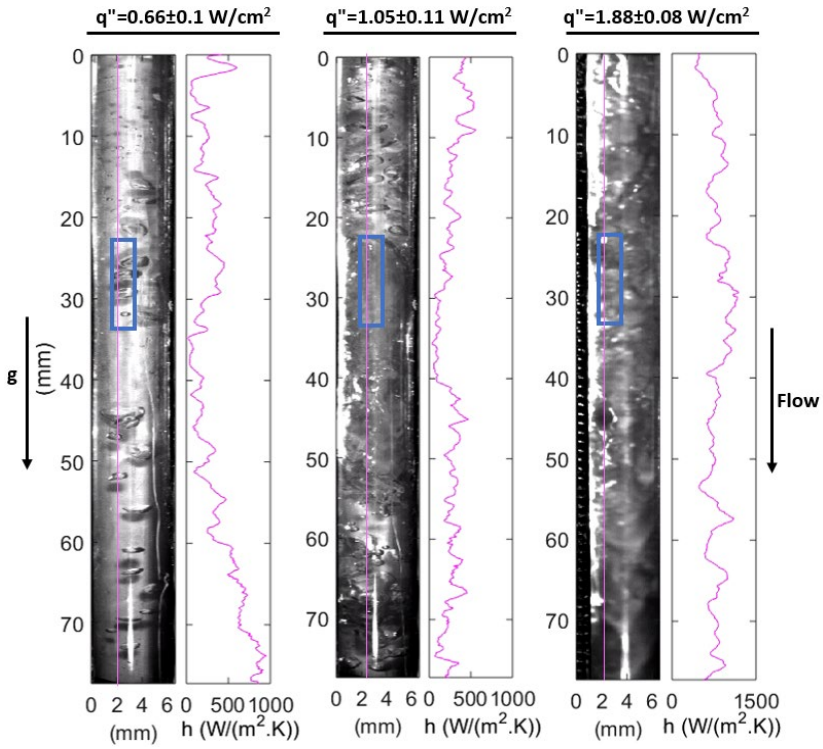

Figure 3.10: Downward flow: heat transfer coefficients for G=40 kg/(m^2.s).

3.2 EFFECT OF GRAVITY

At low heat and mass flux, the gravity level significantly affected the bubble size, shape, and bubble slip velocity (Figure 3.11). In 1.8g, the bubbles were small and spherical. When the gravity level decreased, the buoyancy force decreased, the nucleation site density increased, and bubbles became larger. In microgravity, the bubbles were large, spherical,

and had a high rate of coalescence due to the small slip velocity. In downward flow, bubbles were deformed and flattened. They grew, coalesced, and moved against the flow.

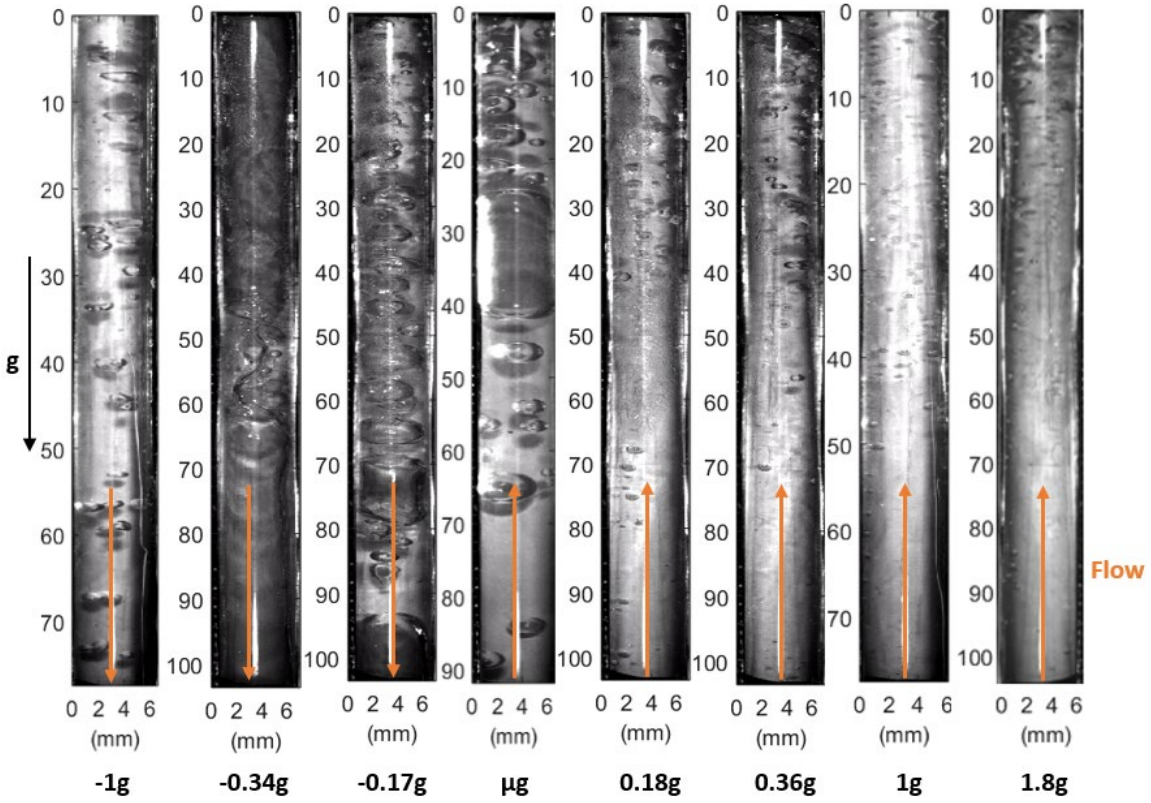

Figure 3.11: Gravity levels comparison: visualization for G=40 kg/(m^2.s) and q" = 0.64±0.1 W/cm^2.

The patterns observed in the local wall heat flux at different gravity levels for bubbly flow (Figure 3.12) can be qualitatively attributed to different heat transfer mechanisms. The small areas of high heat flux behind the bubbles observed in downward flow are strong evidence that turbulent mixing occurs where bubbles are present. There is a noticeable lack of locally varying heat transfer for microgravity, implying that there is weak turbulent mixing heat transfer in microgravity bubbly flow. This contradicts the assumption that an increase in bubble size causes an increase in turbulence. The weak

turbulent mixing in microgravity is attributed to the small/negligible slip velocity. In upward flow, the small areas of high heat flux were due to the different nucleation sites.

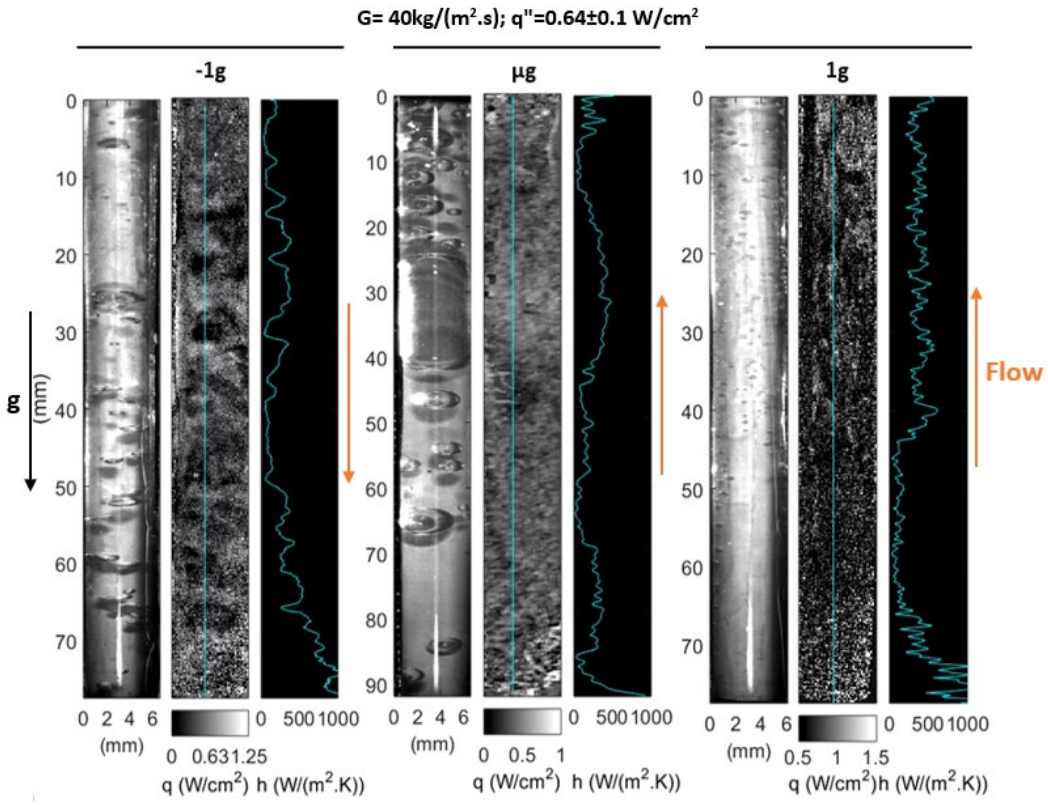

Figure 3.12: Gravity levels comparison: evolution of the flow, heat transfer distribution, and heat transfer coefficient for G=40 kg/(m^2.s) and q"=0.64±0.1 W/cm^2 (left -1g, center μg, right 1g).

The average heat transfer coefficients for the different mass fluxes and heat fluxes at 10.1°C of subcooling are shown as functions of gravity in Figure 3.13. The heat fluxes shown here were averaged between the measured heat fluxes at constant subcooling across all flow rates and gravity conditions. For low mass flux and low heat flux conditions, the average heat transfer coefficient tended to decrease with decreasing absolute gravity level. The combined effects of the bubble detachment frequency, bubble size, and weak wake mixing explain the reduction in heat transfer coefficient for reduced gravity conditions. This trend was observed for conditions in which the flow regime was bubbly flow across

all gravity levels. In the high mass flux and low heat flux cases, nucleation sites were deactivated, and single-phase flow occurred in cases other than microgravity. The heat transfer coefficient is markedly lower for single phase flow due to the absence of boiling heat transfer. At each mass flux for the highest heat flux (1.81 W/cm^2), the heat transfer coefficient was independent of gravity level due to the flow regime transition into annular flow. Additionally, at each heat flux for the highest mass flux (120 $kg/(m^2.s)$), hydrodynamic forces dominate gravity forces and the heat transfer coefficient was independent of gravity. This implies that the gravity influence on flow boiling is not only a function of mass flux but is also dependent on heat flux. The data for downward flow tend to deviate more from the expected trend due to the complex regime transition behavior (e.g., bubbly flow, oscillating Taylor bubbles, annular flow, and churn flow).

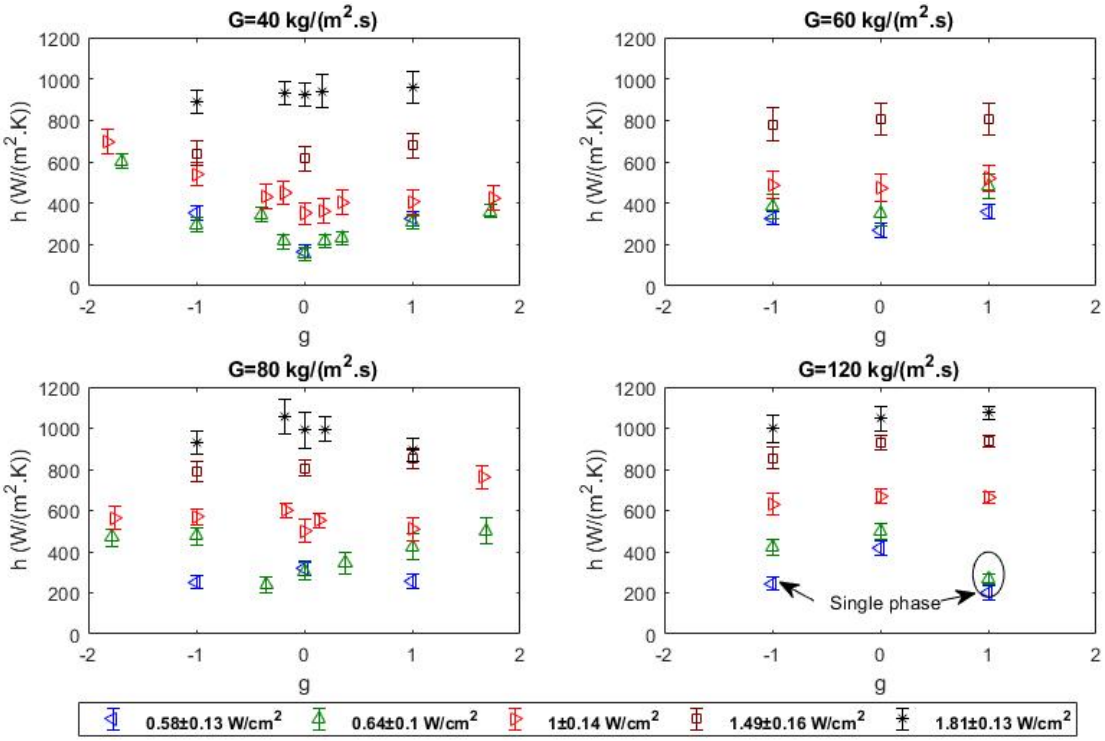

Figure 3.13: Heat transfer coefficient vs. gravity level and mass flux for 10.1°C subcooling.

Regime maps showing the heat transfer coefficient dependence on gravity are shown in Figure 3.14 for 10.1°C and 4.2°C of subcooling. Each condition is notated as either "Gravity Dependent" or "Gravity Independent" at constant mass and heat flux. The criteria for determining gravity dependence was whether the heat transfer coefficients varied by more than ±10% from the average over the gravity levels tested. Conditions which include at least one instance of single-phase flow are additionally marked "Single Phase." The dashed lines shown in Figure 3.14 represent the approximate boundaries between the gravity independent and gravity dependent zones. The large region of gravity dependence at low mass fluxes (pool boiling) is expected due to the presence of natural convection. Significant gravity effects have been observed in pool boiling at high enough heat fluxes due to the change in bubble detachment behavior (Raj et al. [17]). For increasing

mass flux, the effect of natural convective cooling and buoyancy is dominated by forced convection. At moderate mass flux and low heat flux, gravity dependence is due to boiling occurring in microgravity and not in terrestrial gravity. At high enough mass flux and low heat flux, single-phase flow is expected across all gravity conditions, resulting in a gravity independent region. For increasing heat flux, the rapid regime transition to annular flow observed across all gravity levels results in gravity independence. The primary heat transfer mechanism in annular flow is liquid film heat transfer, which varies only slightly with respect to gravity. Lower subcooling levels exhibit a larger range of heat flux conditions in which gravity plays a significant role in affecting heat transfer coefficient. This is due to the increased buoyancy force associated with the larger bubbles observed at lower subcooling. The upper limit of mass flux for gravity dependence for each subcooling is expected to be slightly higher than our tested data.

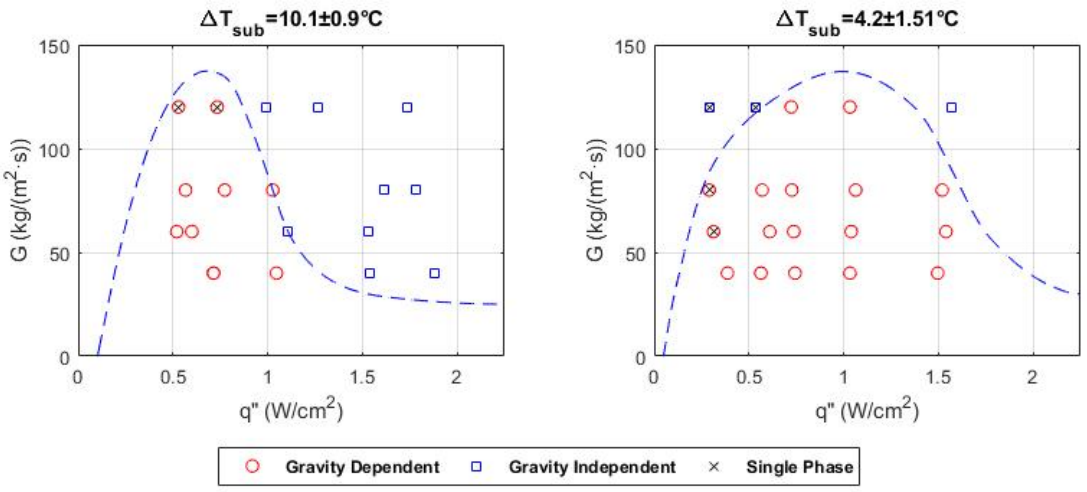

Figure 3.14: Gravity dependence regime maps.

3.3 SUMMARY OF CONTRIBUTIONS

The efficacy of a technique to measure flow boiling wall temperature, wall heat flux, and heat transfer coefficient using TSP was shown for HFE-7000 flowing through a 6 mm ID tube. Local heat transfer coefficient data were recorded for various flow rates, heat fluxes, and gravity levels, including microgravity, partial gravity and hyper gravity. Heat transfer coefficient was shown to increase with increasing flow rate and heat flux at all gravity levels. Changes in flow regime from bubbly to slug to annular flow are dominated by increasing heat flux. In the bubbly flow regime, heat transfer decreases as absolute gravity level decreases. Regime transition in downward flow boiling is complex due to competing hydrodynamic and buoyancy forces. It was observed that the onset of nucleate boiling in microgravity is observed at higher mass fluxes and lower heat fluxes when compared to terrestrial gravity due to the absence of natural convection. The increase in bubble size seen at reduced gravity levels shows low turbulent mixing, contrary to the common assumption that increased bubble sizes leads to increased turbulence. Gravity independence in heat transfer coefficient is shown to be a function of wall heat flux and mass flux. At high heat fluxes, annular flow is observed across all gravity conditions and the heat transfer is constant at all gravity levels due to the domination of film boiling heat transfer.

CHAPTER 4: MODELING CONSIDERATIONS

Conventional vertical flow boiling through a tube includes bubbly flow, slug flow, churn flow, annular flow, and mist flow. The heat transfer mechanisms for each regime are typically well understood for most fluids in terrestrial gravity (Carey [29]). These regimes can be predicted using the quality, the superficial liquid velocity, and the superficial vapor velocity. Large, repeatable datasets have been acquired for 1g upward flow boiling of many fluids and have been used to verify these models. Limited experiments have been performed in microgravity for flow boiling to this extent. The datasets available for microgravity typically only exhibit bubbly flow, slug flow, and annular flow.

Research in microgravity two-phase flow was performed to evaluate the liquid turbulence and forces acting on the gas phase in microgravity two-phase flow (Takamasa et al. [30]). The slip velocity was suspected to vanish in microgravity due to the lack of buoyancy force as shown by McQuillen et al. [31] and Colin et al. [32]. Two phase flows in gravity fields have much higher turbulence due to slip effects which cause wakes behind bubbles. A model which can account for these effects is the drift-flux model which takes into account the relative velocity between phases through a constitutive relation. Ishii [33] developed a correlation for the distribution parameter in upward fully developed bubbly flow that accounts for the interfacial geometry, the body-force field, shear stresses, and the interfacial momentum transfer. Experimental data in various flow regimes and a wide range of flow parameters were obtained. Hibiki and Ishii [34] modified the constitutive equation of the distribution parameter for vertical upward bubbly flow based on a detailed analysis of the bubble dynamics. The momentum interaction between phases was affected by the wall shear stress, which could be applied to microgravity conditions (Hibiki et al. [35]).

Single-imaging and stereo-imaging methods were used to measure the axial developments of flow parameters such as void fraction, interfacial area concentration, and bubble Sauter mean diameter. Unfortunately, the drift-flux model could not be used in the current work since the vapor quality at the center of the tube was negative for 80% of the data acquired in Lebon et al. [18], i.e., the flow was thermodynamically subcooled. Proposed models for each of the three observed regimes are based on observations made using data from Lebon et al. [18].

4.1 BUBBLY FLOW

Since the slip velocity in microgravity flow boiling is zero, a homogeneous two-phase model can be applied (Carey [29]). The defining facet of a homogeneous two-phase model is that the mean liquid and mean vapor velocities are equal. This model takes the following parameters into account:

$$G = \frac{\dot{m}}{A} \tag{8}$$

$$\alpha = \frac{A_v}{A} \tag{9}$$

$$A = A_v + A_l \tag{10}$$

$$\dot{m} = \dot{m}_v + \dot{m}_l \tag{11}$$

$$x = \frac{\dot{m}_v}{\dot{m}} \tag{12}$$

Where G is the mass flux, α is the void fraction, A is the cross-sectional area, ṁ is the mass flow rate, and x is the quality. Combining and rearranging these terms, one can define the

phase superficial velocities and the phase mean velocities, j and u respectively. The equivalency between the mean liquid and mean vapor velocities can be used to solve for α as a function of x.

$$j_v = \frac{Gx}{\rho_v} \tag{13}$$

$$j_l = \frac{G(1-x)}{\rho_l} \tag{14}$$

$$u_v = \frac{Gx}{\rho_v \alpha} \tag{15}$$

$$u_l = \frac{G(1-x)}{\rho_l(1-\alpha)} \tag{16}$$

$$\alpha = \frac{x/\rho_v}{[(1-x)/\rho_l] + (x/\rho_v)} \tag{17}$$

It is hypothesized that the local heat flux in microgravity bubbly flow can be obtained through the effects of liquid convection alone due to the negligible slip velocity in microgravity. Heat added to the fluid causes bubbles to expand as they travel along the tube, and conservation of mass dictates that the fluid accelerates as more vapor becomes present. The liquid velocity could be attained if the quality and void fraction are both known, which can be modeled using the above relations. The liquid velocity could then be used in single-phase heat transfer correlations such as Shah & London [25]. The data from Lebon et al. [18] cannot be used to verify these models since most of the data is thermodynamically subcooled (i.e. negative quality). Additional saturated microgravity flow boiling data is needed to verify these models. Void fraction probes at the inlet and outlet of the heated test section could also be used to validate the model.

4.1.1 Preliminary Validation

The feasibility of modeling microgravity flow boiling heat transfer using single-phase estimations of an accelerating flow was determined using an alternative visual method to study subcooled data. The proposed approach was to compare microgravity flow boiling experiments through a straight tube with single-phase flow simulations of flow within a tube of varying diameter that recreates the experimentally obtained local liquid velocity. The liquid velocity along the tube for data from Lebon et al. [18] was obtained by tracking the velocities of isolated small bubbles and correcting for any residual buoyancy force. The fluid acceleration was accounted for by modeling a tube with shrinking diameter in ANSYS Fluent. The inlet mass flux, heat flux, and subcooling values were matched to experimental values, and the resulting heat transfer simulation data were compared to experimentally acquired data.

Small bubbles with diameters of 0.3 mm or lower were identified and tracked during flow boiling to obtain the local liquid velocity profile. For single-phase flow through a tube with a fully developed laminar velocity profile, the local velocity as a function of radius at a point z along the tube axis can be determined by the parabolic profile shown below:

$$v_{lam} = 2v_m\left(1 - \frac{r^2}{r_{max}^2}\right) \tag{18}$$

The assumption of negligible slip velocity implies bubbles travel at approximately this local liquid velocity. Since the radial location of the bubble could not be determined from our single flow visualization camera, the velocities of many bubbles were tracked and averaged at specific axial locations, and a statistical analysis was used to calculate the

uncertainty in the measured average velocities. The number of velocity samples needed to accurately capture their average was quantified in order to account for the unknown radial location. The uncertainty in the average velocity from a group of randomly seeded points within a laminar velocity profile was estimated using a Monte Carlo simulation. The parabolic velocity profile in equation 18 was constructed in Matlab as a function of r, with a maximum radius r_{max} and maximum velocity $2v_m$ of 1 to obtain normalized results. A number of velocities n were sampled at random radial locations in order to simulate the positions of passing bubbles, then averaged to obtain a simulated average velocity. This was repeated 100,000 times to obtain a distribution of velocities from which a standard deviation was computed for each n. The uncertainty was then represented as a percent error between the simulated average velocity and the actual average velocity v_m with 95% confidence shown in Table 4.1. For our experimental measurements, at least 10 bubble velocities were used.

Table 4.1: Average visually tracked velocity Monte Carlo error analysis.

Number of points *n*	**Normalized Standard Deviation ($v/2v_m$)**	**Percent Error (95% Confidence)**
5	0.129	51.5%
10	0.0913	36.5%
25	0.0579	23.2%
50	0.0407	16.3%
100	0.0289	11.6%

To account for small fluctuations in gravity level and its effect on the measured bubble velocity, we considered a stationary, spherical bubble that was suddenly released within a stationary liquid in a gravity field. For the small bubbles that were used to

determine the local liquid velocity (D_{bu}~0.3 mm) and the aircraft g-jitter levels (-0.03<a/g<0.05), the bubble Reynolds number was small and inertial forces could be neglected compared to buoyancy and viscous forces. A simple force balance on the bubble was used to estimate the bubble rise speed:

$$F_B - F_D = m_{bu}\frac{dv_{bu}}{dt} \tag{19}$$

where the buoyancy and drag forces are given by $F_B = (\rho_l - \rho_v)gV_{bu}$ and $F_D = \frac{1}{2}\rho_l v_{bu}^2 C_D A_{bu}$ respectively. The force exerted on the bubble due to two-phase pressure gradient was found to be negligible. For the largest pressure drop of 56.4 Pa/m observed in this work, the pressure force experienced by bubbles with diameters of 0.3 mm is on the order of $F \sim 10^{-9}$ N, which is much smaller than the typical buoyancy force, $F_D \sim 10^{-7}$ N.

There are many expressions through which the drag coefficient C_D can be estimated, most of which are based on data obtained at much higher bubble Reynolds numbers. Since small bubbles have been found to behave like solids (e.g., Bond and Newton [36], Wallis [37]), the drag coefficient was assumed to be $C_D = \frac{24}{Re_{bu}}$ (Re<1). This simple relation also enabled a closed form solution for bubble velocity to be obtained. With these assumptions, the bubble velocity was shown to be:

$$v_{bu}(t) = v_t[1 - \exp(-t/\tau)] \tag{20}$$

where $v_t = \frac{(\rho_l - \rho_v)gD_{bu}^2}{18\mu_l}$ is the bubble's terminal velocity and $\tau = \frac{\rho_v D_{bu}^2}{18\mu_l}$ is the time constant. For the experimental conditions in this work, $\tau = 10^{-4}$ s, indicating we could assume the bubbles moved at the terminal velocity. Terminal velocities between -4.5 mm/s<v_t<7.5 mm/s were obtained for our conditions and subtracted from the measured bubble velocities

to obtain corrected local liquid velocities. The corrected liquid velocity vs. the measured bubble velocity shown in Figure 4.1 shows that the correction for the data was less than 10% for the great majority of cases, indicating accurate relations for C_D were not needed. The largest uncertainty in the correction for gravity effects was 1.5 mm/s, which was negligible compared to the measurement uncertainty. The average bubble terminal velocity was 4% of the average bubble velocity within the tube reference frame, i.e., the hydrodynamic forces dominated the buoyancy force and inertial forces were negligible.

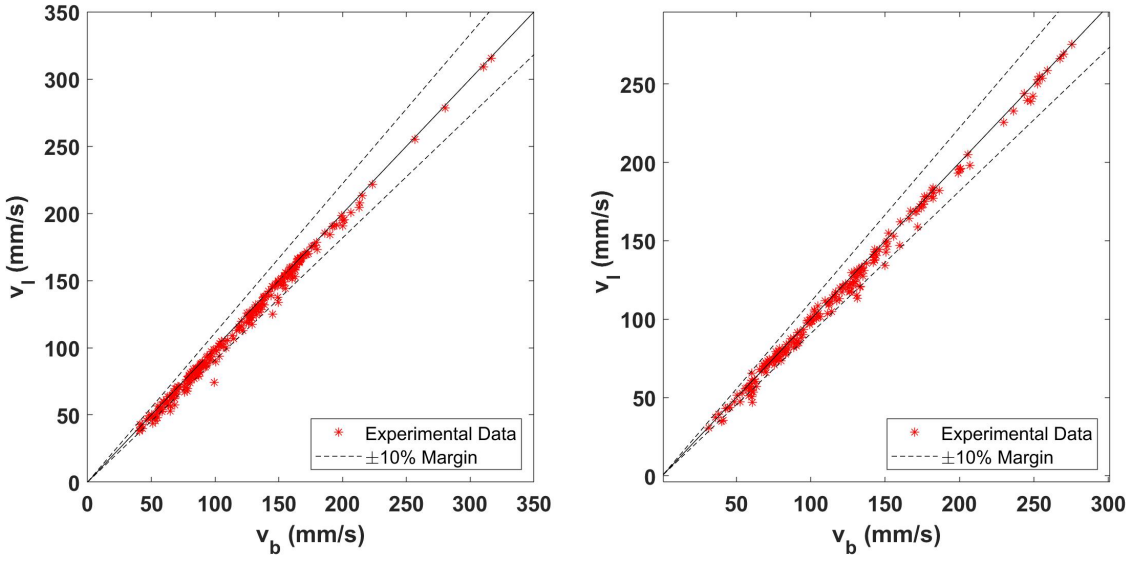

Figure 4.1: Corrected liquid velocity (v_l) vs. measured bubble velocity (v_b) for all cases at ΔT_{sub}=10.1°C (left) and ΔT_{sub}=4.2°C (right).

The bubble velocity profile along the tube is then used to compute the shape of a tube with shrinking diameter to match the experimental profile. The shape of the tube D(z) was computed from the liquid velocity profile $v_l(z)$ using a mass balance which reduces to $D(z) = \sqrt{\frac{D_{in}^2 v_{in}}{v_l(z)}}$ where D_{in} and v_{in} are the inlet tube diameter and inlet velocity, respectively. The liquid velocity and tube profile for a low mass and heat flux case (G=39 kg/(m^2.s), q"=0.48 W/cm^2, ΔT_{sub}=9.0°C) are shown on Figure 4.2 as an example. The curve

fits to the liquid velocity and diameter data indicated by the solid lines were forced to include the inlet velocity of 30 mm/s and inlet diameter of 6 mm at z=0 mm. The fitting process was repeated for the upper and lower limits of the liquid velocity error bars to obtain the uncertainty in the fitted liquid velocity, which are indicated by the "+" and "-" subscripts. These uncertainty curve fits for velocity were propagated to the diameter profiles, shown by D_+ and D_-. The liquid velocity at the tube exit was over three times the inlet velocity for this case which illustrates the strong acceleration the flow can undergo in the axial direction due to bubble formation. Figure 4.3 schematically illustrates tube profiles for the experimental two-phase flow and the equivalent, simulated single-phase flow.

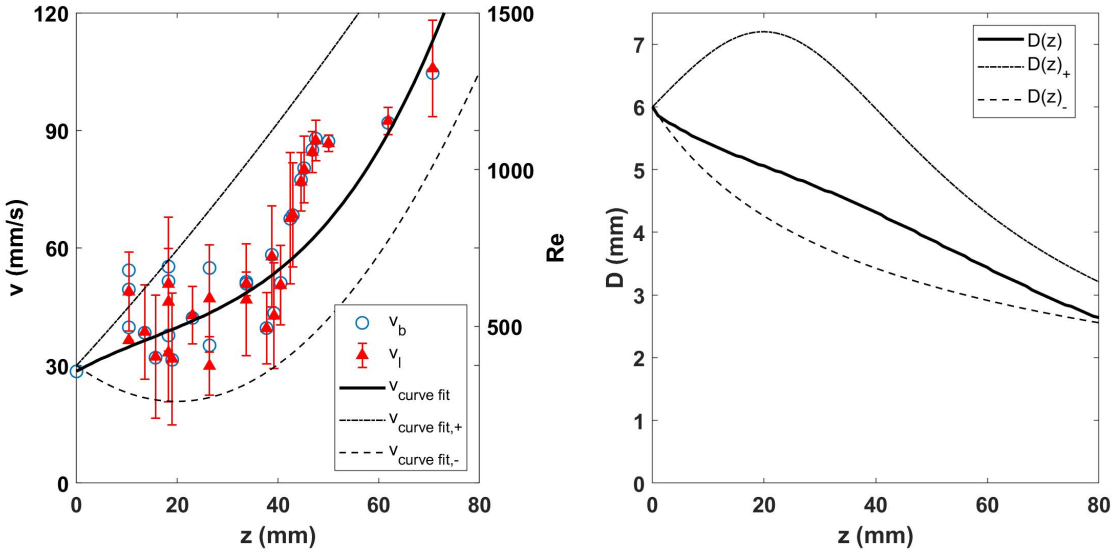

Figure 4.2: Liquid velocity profile (left), and tube diameter (right) for G=39 kg/(m^2.s); q"=0.48 W/cm^2; ΔT_{sub}=9.0°C.

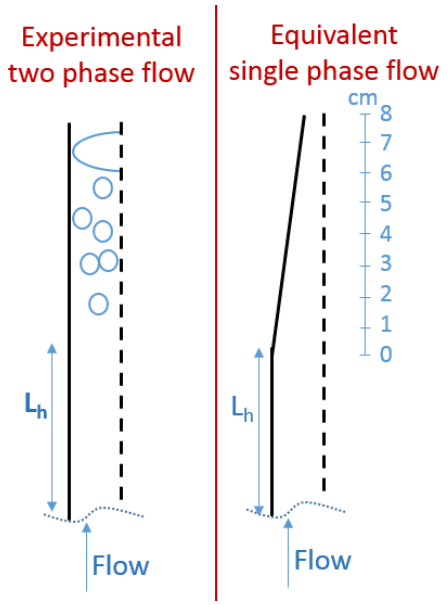

Figure 4.3: Schematic of experimental (left) and numerical (right) tube profiles.

The tube profiles were imported into ANSYS Fluent along with the measured wall heat flux distribution so the local heat transfer coefficient could be computed as a 2-D axisymmetric, single-phase flow. The fluid domain was constructed in ANSYS DesignModeler using a 2-D mesh. The inlet velocity, outflow, and wall heat flux of the fluid domain were imposed as values acquired from microgravity experiments. The heated test section was preceded by an unheated flow development section of length 330 mm to match the experimental conditions. For Re=1100, the hydrodynamic entry length was 330 mm, so cases with flow rates below this Reynolds number were hydrodynamically fully developed at the inlet of the test section. The regressed tube diameter profiles ($D_+(z)$ and $D_-(z)$) were imported into ANSYS separately to deduce the uncertainty of the numerical results. The uncertainty associated with the velocity resulted in an uncertainty in wall heat transfer coefficient of about 10-20%.

Model validation was performed by simulating flow through a straight tube (D(z) is constant) preceded by an unheated flow development section of length 1 m. This entry length ensured the simulated flow was hydrodynamically fully developed, which was verified by observing a parabolic velocity profile at the beginning of the heated tube. Heat transfer coefficients along the heated tube length were computed for cases of constant wall heat flux (h_Q) and constant wall temperature (h_T). Figure 4.4 compares the results to the analytical solutions for hydrodynamically fully developed, thermally developing flow through a straight tube for their respective cases given in Kays et al. [38]. The numerical results with constant wall heat flux had an RMS error of 3.6%, while the numerical results with constant wall temperature had an RMS error of 5.5%.

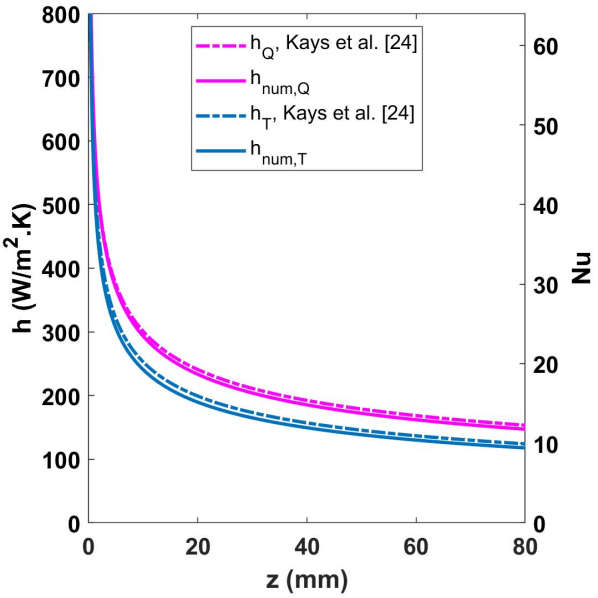

Figure 4.4: Validation of numerical heat transfer coefficients for cases of constant wall heat flux (h_Q) and constant wall temperature (h_T).

The following experiments were simulated using laminar flow since the single-phase Reynolds number was below 2300 along the entirety of the tube length for each case. High mass flux at low heat flux can deactivate nucleation sites and cause single-phase flow,

which was observed in the high flow rate, low heat flux case (Figure 4.5, right). In this case, the uncertainty was only associated with the flowmeter, thermocouple, and heater power errors. Since there were no bubbles, the flow acceleration due to bubble expansion was zero and the simulated heated tube was assigned a straight profile. The single-phase numerical and microgravity experimental heat transfer coefficients (h_{num} and $h_{exp,\mu g}$, respectively) are shown in Figure 4.5, along with the single-phase, hydrodynamically fully developed, constant wall heat flux solution from Kays et al. [38]. The microgravity experimental data (local, time-averaged heat transfer coefficient) are in good agreement with the numerical prediction of the heat transfer coefficient in the adjusted tube profile within the simulated error margins ($h_{num,+}$ and $h_{num,-}$). When compared to the analytical solution from Kays et al., the data and the numerical simulation are slightly lower at the inlet and slightly larger at the outlet. This is due to the insufficient development length preceding the heated tube for the experiment and simulation at this Reynolds number. 1g upward flow heat transfer coefficient data for the same conditions taken from Lebon et al. [18] are also shown, and indicate terrestrial heat transfer coefficients ($h_{exp,1g}$) were slightly higher due to the presence of natural convection.

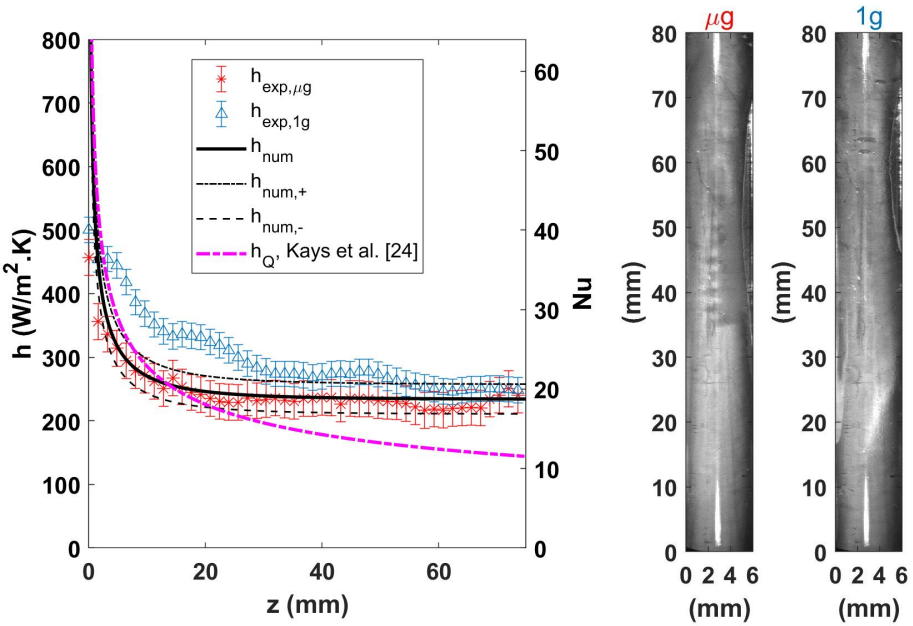

Figure 4.5: Comparison of experimental, numerical, and correlation heat transfer coefficients (left) and visual snapshot of single-phase flow (right) for: G=122 kg/(m^2.s); q"=0.31 W/cm^2; ΔT_{sub}=5.6°C.

Comparisons between the numerical and experimental heat transfer coefficient data along the length of the heated tube are shown in Figures 4.6 and 4.7 for the moderate heat flux cases. The microgravity experimental data are also in good agreement with the numerical prediction of the heat transfer coefficient for these conditions. The numerical single-phase simulation of a straight tube ($h_{num,str}$) is also shown for each case at the respective conditions. For the higher mass flux conditions in the moderate heat flux case (Figure 4.6), there was little deviation from the straight tube simulation since nucleation occurred further down the tube and the bubble departure diameters were smaller, resulting in less flow acceleration. For the low flow rate case (Figure 4.7), the numerical single-phase simulation of a straight tube is seen to underpredict the experimental data near the tube outlet by about 50%, indicating the need to account for the local flow acceleration.

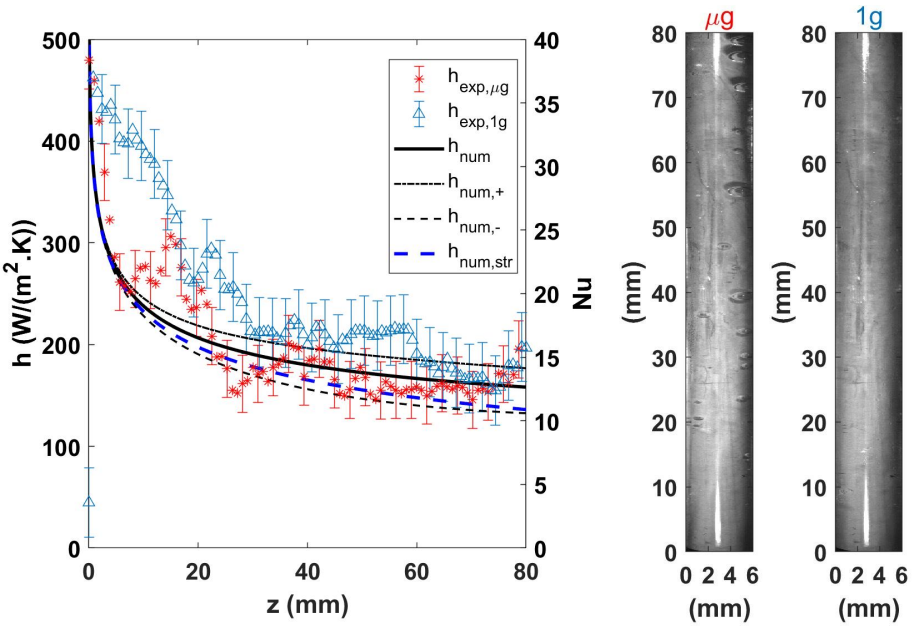

Figure 4.6: Comparison of experimental and numerical heat transfer coefficients (left) and visual comparison of 1g upward and microgravity flow boiling (right) for G=123 kg/(m^2.s); q"=0.63 W/cm^2; ΔT_{sub}=9.5°C.

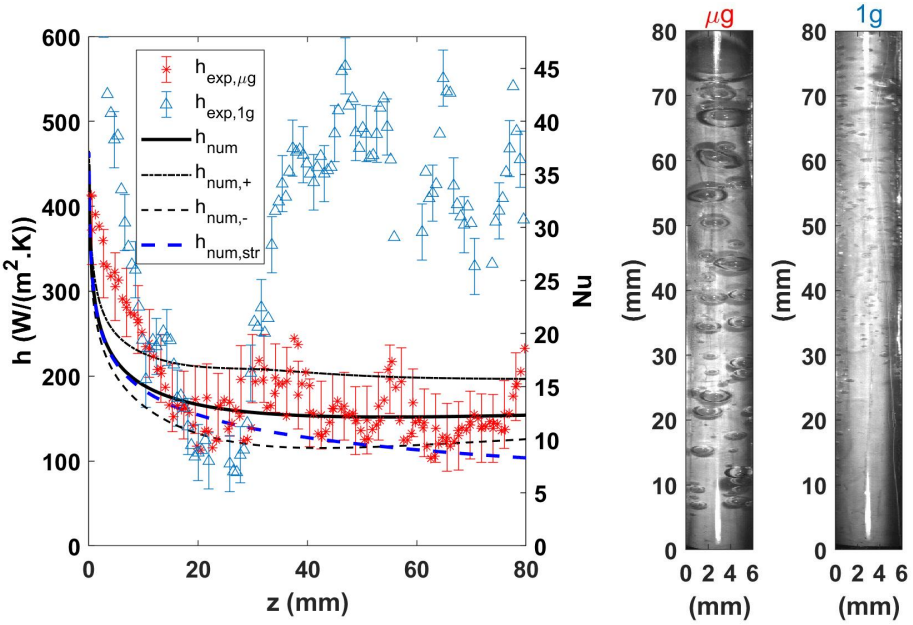

Figure 4.7: Comparison of experimental and numerical heat transfer coefficients (left) and visual comparison of 1g upward and microgravity flow boiling (right) for G=39 kg/(m^2.s); q"=0.48 W/cm^2; ΔT_{sub}=9.0°C.

To compare the difference between microgravity bubbly flow and terrestrial upward bubbly flow, data from Lebon et al. [18] are also shown on Figures 4.6 and 4.7 for the same experimental conditions as shown. In upward flow on Figure 4.6, nucleation sites were deactivated and single-phase flow occurred due to the high mass flux and low heat flux. In upward flow on Figure 4.7, the flow entered the bottom of the tube as subcooled liquid, and the heat transfer coefficient decreased as the thermal boundary layer developed. A jump in heat transfer occurred due to two-phase turbulent mixing once nucleation was initiated at approximately z=25 mm. The heat transfer coefficients observed in upward flow boiling were about three times larger than they were in microgravity flow boiling even though the bubbles in microgravity flow were much larger. In microgravity, only inertial forces aided bubble detachment against capillary forces (Colin et al. [27]), allowing bubbles to grow much larger before detaching.

It is feasible to predict microgravity isolated bubbly flow boiling heat transfer using single-phase heat transfer models if the local axial velocity is used. Microgravity bubbly flow boiling heat transfer could be predicted using single-phase laminar simulations and the local liquid velocity if the liquid remains laminar (low Reynolds numbers and no bubble coalescence). The dominant heat transfer mechanism in these cases was laminar forced convection since there was little wake mixing around the bubbles.

4.2 SLUG FLOW

Vapor slugs are observed in microgravity flow boiling as large bubbles begin to coalesce. These vapor slugs are separated by liquid slugs which may have additional bubbles dispersed throughout. The dominant heat transfer mechanism around the vapor slug is thin film evaporation. Rapid expansion of slugs occurs as the thin film evaporates. This causes

the head of the slug to accelerate much quicker than the tail relative to the tube. The elongated thin liquid film moves slowly due to the small shear force exerted by the vapor core. As the liquid film evaporates, there is a significant risk of dryout at the wall since liquid is not being actively replenished. This could be a cause of critical heat flux even at moderate heat fluxes in microgravity.

A model which can be attributed to microgravity slug flow is a modified Kandlikar correlation used for microchannel evaporation shown in equations 21-24 [29]. The maximum of nucleate boiling dominated heat transfer h_{NB} and convective boiling dominated heat transfer h_{CB} is taken as a modification of the heat transfer of the liquid as if it were flowing alone through the tube, h_l.

$$h = \text{maximum of } \begin{cases} h_{NB} \\ h_{CB} \end{cases} \tag{21}$$

$$h_{NB} = 0.6683 \left(\frac{\rho_l}{\rho_v}\right)^{0.1} x^{0.16}(1-x)^{0.64} h_l + 1058.0 Bo^{0.7} F_K (1-x)^{0.8} h_l \tag{22}$$

$$h_{CB} = 1.1360 \left(\frac{\rho_l}{\rho_v}\right)^{0.45} x^{0.72}(1-x)^{0.08} h_l + 667.2 Bo^{0.7} F_K (1-x)^{0.8} h_l \tag{23}$$

$$h_l = \left(\frac{k}{D}\right) \frac{(Re-1000)Pr(f_i/2)}{1+12.7\left(Pr^{2/3}-1\right)(f_i/2)^{0.5}} \tag{24}$$

F_K is a constant that varies between fluids. Values for F_K are listed in Carey [29]. Since the Bond number approaches zero in microgravity, the criteria for microchannel feasibility is satisfied. This is verified by data from Lebon et al. [18] where it has been observed that bi-directionally expanding slugs form at moderate heat fluxes similar to microchannel bubble behavior. These slugs fill the entirety of the tube and tend to exhibit similar heat flux to microgravity bubbly flow cases. This bodes well for the proposed model, which posits that

single-phase heat transfer dominates, but additional microgravity data with prevalent slug flow is necessary to fully understand the heat transfer mechanism effects at different heat and mass fluxes.

4.3 ANNULAR FLOW

Annular flow is characterized by a continuous vapor core surrounded by a continuous liquid film. The literature remarks about annular flow liquid film thickness in microgravity are inconsistent. Ohta [5] observed thicker liquid films and argues that this is due to the reduced shear stress exerted on the liquid film. Narcy et al. [7] observed thinner liquid films in microgravity and claim that the reduced body force on the liquid causes it to stretch thinner. The differences could be due to sensitivities to working fluid properties or flow rates, but further research needs to be completed on the definitive film thickness response to change in gravity. Annular flow is also characterized by disturbance waves, which are caused by instabilities at the liquid-vapor interface. The passage of these disturbance waves causes the liquid film to fluctuate in thickness. Troughs in the disturbance waves could create breaks in the liquid film as it is evaporating and locally dry the fluid. This is a cause of critical heat flux in annular flow, but it may occur at higher heat fluxes in microgravity due to the increased liquid film thickness.

A physical model for annular flow in a vertical round tube with no entrainment is given in Carey [29]. This model could be used as a first approximation for microgravity annular flow boiling by analyzing the velocity profile within and thickness of the liquid film. The model involves a steady state force balance of shear stress, pressure, and gravitational body forces at a given location within the liquid film. The assumptions within the model are that the flow is steady, the downstream pressure gradients felt in the core and

the liquid film are the same, and the liquid flows in an annular film on the inside wall of the tube that has a uniform thickness δ and a smooth liquid-vapor interface. The model can be applied using specified fluid properties and flow parameters. The equations used to solve the model are shown below:

$$\tau_i = \frac{f_i G^2 x^2}{2\rho_v \alpha^2} \tag{25}$$

$$f_i = 0.005\left(1 + 300\frac{\delta}{D}\right) \tag{26}$$

$$\frac{dP}{dz} = -\frac{4\tau_i}{D} - \frac{2xG^2}{\alpha^2\rho_v}\left(\frac{dx}{dz}\right) - \rho_v g \tag{27}$$

$$\frac{dx}{dz} = \frac{4q''}{GDh_{fg}} \tag{28}$$

$$\varepsilon = n^2 uy\left(1 + e^{-\rho_l n^2 uy/\mu_l}\right) \tag{29}$$

$$\frac{du}{dy} = \frac{\tau_i}{\mu_l + \varepsilon\rho_l}\left(\frac{D/2-\delta}{D/2-y}\right) + \frac{1}{2}\left(\frac{dP}{dz} + \rho_l g\right)\left(\frac{D/2-y}{\mu_l + \varepsilon\rho_l}\right)\left[\left(\frac{D/2-\delta}{D/2-y}\right)^2 - 1\right]$$
$$at\ y = 0: \quad u = 0$$
$$at\ y = \delta: \quad \frac{du}{dy} = \frac{\tau_i}{\mu_l + \varepsilon\rho_l} \tag{30}$$

$$\left(\frac{D}{4}\right)G(1-x) = \rho_l \int_0^\delta u dy \tag{31}$$

Equation 25 defines the interfacial shear stress τ_i at the liquid-vapor interface and requires the friction factor f_i to solve. The friction factor is defined by a correlation proposed by Wallis [39] shown in equation 26. The pressure drop is given by equation 27, and the rate of change in quality is given by equation 28. An eddy diffusivity is required to form closure within the model, and the model chosen is the Deissler correlation given in

equation 29, where n is a constant equal to 0.1. These equations are needed to solve the velocity profile within the liquid film shown in equation 30, where y is the distance from the tube wall to the liquid-vapor interface. An iterative procedure is required to solve these equations, since the film thickness δ is treated as both an input as well as a verification for the system in the form of a mass balance shown in equation 31. The total liquid mass flow must match the integrated mass flow of the liquid velocity profile solved by equation 30.

The resulting film thickness and liquid velocity profile can be used in conjunction with annular flow heat transfer models to predict microgravity flow boiling heat transfer. The predominant characteristics of annular flow are similar between microgravity and terrestrial gravity, however further study needs to be performed on the frequency and depth of passing disturbance waves to truly characterize the heat transfer.

4.4 SUMMARY OF CONTRIBUTIONS

Models have been proposed for microgravity bubbly flow, slug flow, and annular flow based on the observation of negligible slip velocity. Preliminary validation of the bubbly flow model was performed by simulating a tube with a single-phase accelerating flow. The increase in velocity was tuned to match experimental microgravity bubbly flow boiling cases where small bubbles were tracked to identify the local average velocity. Good agreement was observed between simulated single-phase accelerating flows and microgravity bubbly flow boiling local heat transfer. This highlights the dominance of single-phase convective heat transfer in the liquid layer during microgravity bubbly flow boiling. Liquid acceleration due to bubble expansion cannot be considered negligible, and therefore the local axial velocity must be used when modeling the single-phase heat transfer. Modeling assumptions incorporating this finding are also implemented in a slug

flow model that has been developed for microchannel flow boiling, since the low Bond number criterion is met. Finally, an annular flow model taken from Carey [29] is proposed considering liquid film thickness. Additional local saturated flow boiling data are needed to verify these three models.

CHAPTER 5: QUENCHING STUDY

5.1 QUENCHING BACKGROUND

The modeling efforts made in microgravity flow boiling heat transfer can be applied to the chilldown, or quenching, of cryogenic lines aboard spacecraft. Chilldown is the transient process of cooling down transfer lines between cryogen tanks (storage and propulsion systems, resupply). Boiling points of cryogens such as liquid hydrogen and liquid oxygen are significantly lower than room temperature, so a stored cryogen is vaporized when sent through a transfer line due to the several hundred Kelvin temperature difference between the cryogen and the ambient. As seen in Figure 5.1, pure vapor flow or inverted annular flow initially cools the transfer line as the inner wall temperature approaches the Leidenfrost Point. Liquid intermittently rewets the wall in the transition regime until critical heat flux is reached. The flow then enters the nucleate boiling regime, and eventually reaches the desired single-phase liquid flow. The chilldown process is inherently unsteady. Mechanistic understanding of the complex flow boiling phenomena throughout the chilldown process will improve the efficiency of cryogen transfer by minimizing chilldown time and vaporized cryogen amount.

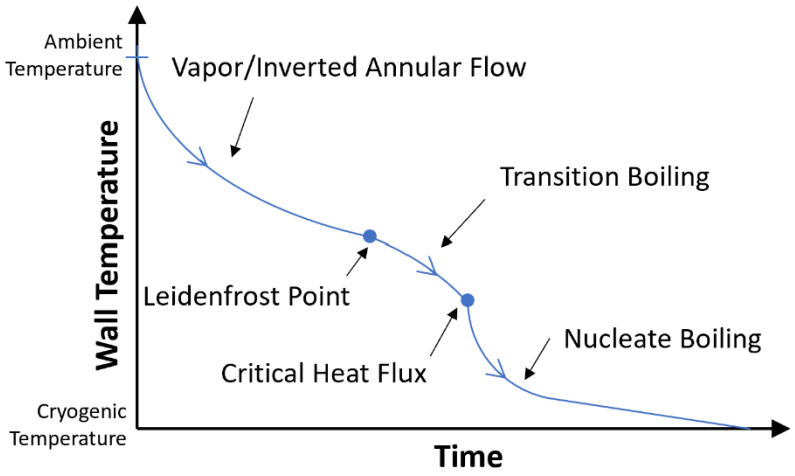

Figure 5.1: Schematic graph of chilldown process.

Research on microgravity cryogen quenching is limited by the infrequent opportunities to gather microgravity data as well as the expense in working with cryogens, making the number of studies even more sparse than microgravity flow boiling. Darr et al. [40] found up to 25% deterioration in microgravity film boiling heat transfer coefficients when compared to terrestrial gravity. They also found that this deterioration diminishes with increasing flow rate, which is to be expected when comparing to flow boiling results. Hartwig et al. [20] evaluated two-phase heat transfer coefficient and critical heat flux correlations using experimentally acquired cryogen quenching data from a variety of sources at terrestrial gravity. Most correlations significantly over-predicted the data, with some correlations off by up to 20,000% in the case of film boiling. Mercado et al. [41] also evaluated two-phase correlations for cryogens undergoing steady state heated tube tests. They found that, even in steady state conditions, two-phase cryogen heat transfer was underpredicted by correlations. The best film boiling correlation under-predicted steady state data by 127%, and the best nucleate boiling correlation under-predicted steady state data by 397%. The authors listed some key reasons why the disparity between correlations

and experimental data could be so large. First, correlations are primarily developed for and tested using room temperature fluids and not cryogens. The scaling of the correlations to cryogenic temperatures may significantly affect the two-phase heat transfer mechanisms. This issue could be rectified by developing a database of microgravity cryogen two-phase heat transfer data to refine correlations, which would be quite expensive and time-consuming. Another issue is that the correlations are derived using steady state data. The quenching process is highly transient, and both the thermal mass of the system and the plays an important role in determining the heat transfer within each flow regime as well as the time it takes to transition between them. The effect of various heating conditions during the chilldown process could be evaluated to determine the transient effects.

The objective of the quenching study is to identify the transient effects within the nucleate boiling regime of the quenching process for HFE-7000. Heated and unheated quenching tests were performed using the existing sapphire tube and TSP measurement test section, and the resulting heat flux and heat transfer coefficient data were analyzed to evaluate whether existing correlations are significantly affected by heating rate during quenching.

5.2 TEST SECTION MODIFICATION

Modifications were made to the flow loop to accommodate a quenching study. A 3-way bypass valve, shown schematically in Figure 5.2, that diverts the flow around the test section was installed. This allows the flow to be cut off from the test section while continuously flowing through the remainder of the loop. The test section can then be heated to vaporize the liquid within the sapphire tube. The inlet of the test section is open to the

rest of the flow loop, preventing significant increase in test section pressure during the vaporization process.

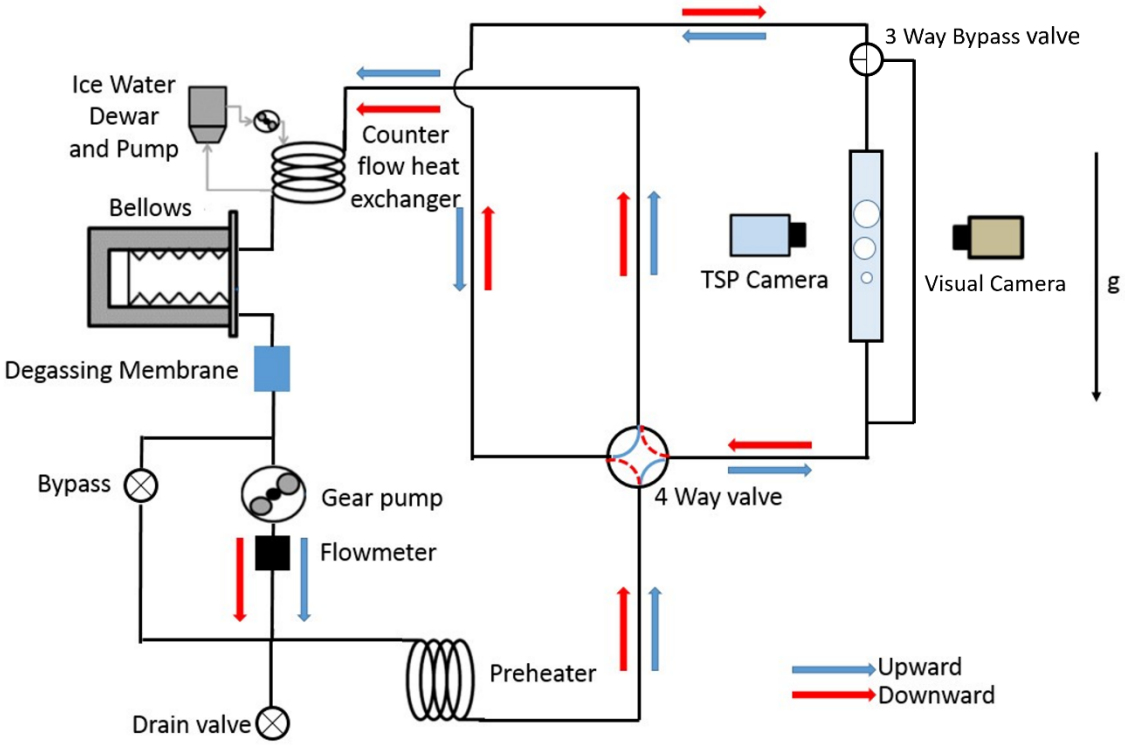

Figure 5.2: Flow boiling test loop with bypass.

The quenching process was initiated by bringing the flow loop to a desired mass flux, rotating the bypass valve to isolate the test section, vaporizing the fluid in the test section, heating the vapor in the test section to a desired temperature, then rotating the bypass valve to allow liquid to quench the test section. Complete vaporization within the test section was confirmed visually before initiating the quench. Three thermocouples were attached to the outside of the sapphire tube at the top, center, and bottom. The center thermocouple at the center was used to determine the test section temperature just prior to quenching. For part of the experiments, the high voltage power supply was turned off just

prior to the quench. This creates a condition where the heating source is cut off at a certain threshold temperature and the tube can cool to single-phase flow. Additional experiments were performed with the high voltage power supply providing heating throughout the entire quenching process so the test section cooled more slowly. These tests are used to compare the test section response to a different cooling condition, and therefore can be used to determine the stability of the quenching process at specific flow rates and initial temperatures.

5.3 EXPERIMENTAL QUENCHING RESULTS

Data was obtained at three mass fluxes (40, 80, 160 kg/(m^2.s)), three nominal initial test section temperatures (~50°C, ~65°C, ~75°C), and two cooling conditions (heater remaining on and heater turning off just before quenching). The heat flux supplied for the cases with persistent heating was 1 W/cm^2. The TSP film temperature data were recorded at 300 Hz for 60 s. Data reduction was performed using the same methods described in Chapter 2.

5.3.1 Wall Temperature and Heat Flux

Figure 5.3 shows the area-averaged wall temperature (blue) and heat flux (red) as a function of time for the case with G = 160 kg/(m^2.s) where the heater was turned off following the quench. The quench occurs at roughly 3.7 s. Before the quench, the temperature was roughly 70°C and the heat flux was 0 W/m^2. The pure vapor flow acts as an insulator while the wall temperature slowly rises due to sensible heating within the sapphire tube. Immediately after the quench, the heat flux rises to 14000 W/m^2 and the temperature drops to roughly 45°C. Figure 5.4 shows a portion of the wall temperature and heat flux for this case just near the time of the quench. The response time of the wall

to the sudden change from vapor flow to nucleate boiling occurs within less than 0.1 s. The slight fluctuations in temperature and heat flux just before the quench are due to brief intermittent wetting of the wall just ahead of the quench front. The heat flux during the nucleate boiling phase rapidly decreases as the wall temperature decreases. All quenching cases tested within this dataset exhibit this behavior after the quench.

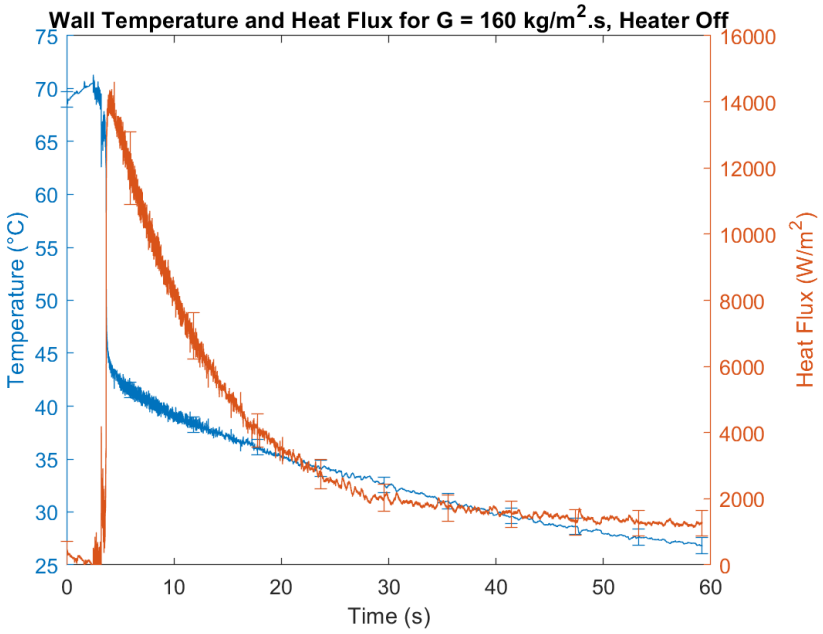

Figure 5.3: Area-averaged wall temperature and heat flux for G = 160 kg/(m^2.s).

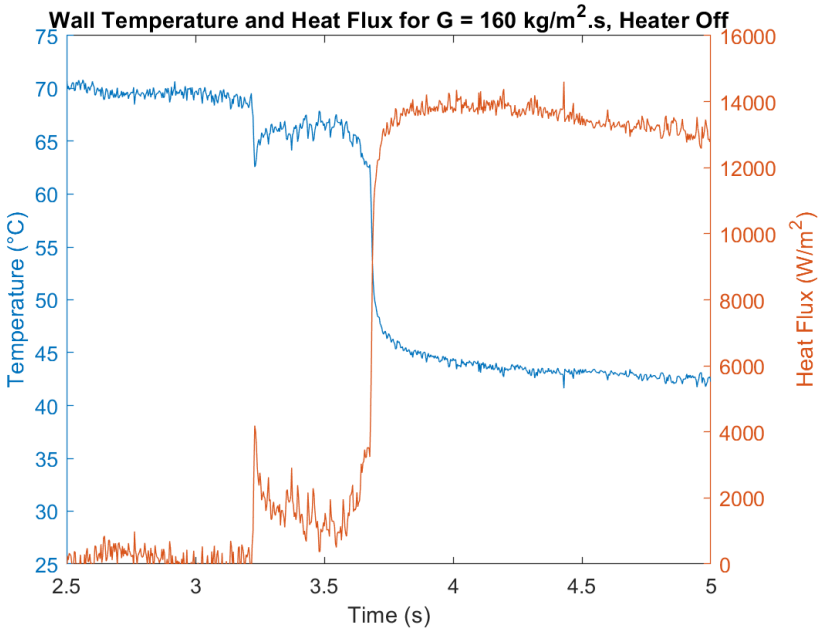

Figure 5.4: Area-averaged wall temperature and heat flux just near quench for G = 160 kg/(m^2.s).

The boiling curves for the cases with G = 160 kg/(m^2.s) at the three nominal initial temperatures are shown in Figure 5.5. The sudden increase in heat flux and decrease in temperature is also apparent here for each initial temperature. The temperature and heat flux data after the quench overlap for each case, indicating the independence of nucleate boiling heat transfer mechanisms in response to different pre-quench temperatures. This conclusion cannot be extended to transitional and film boiling. Much higher temperatures will need to be reached to observe transitional and film boiling behavior.

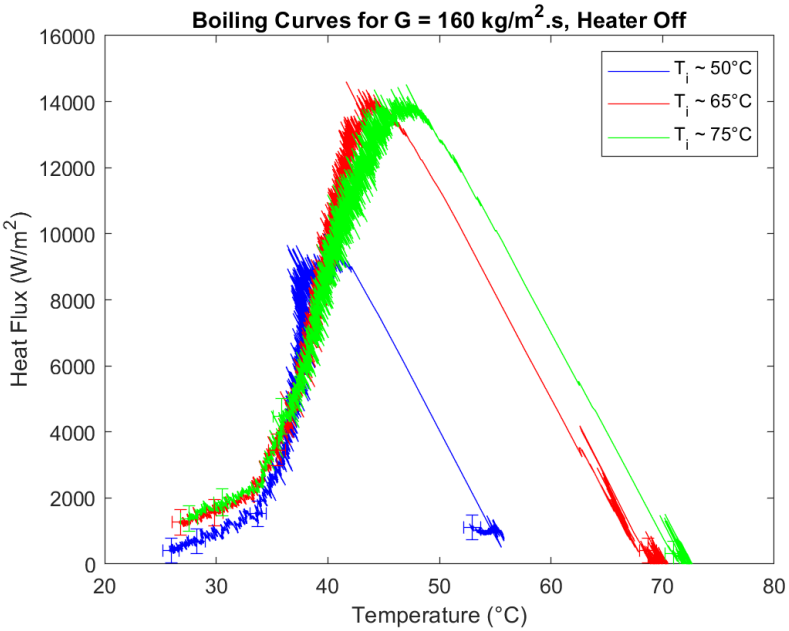

Figure 5.5: Quenching test boiling curves at different initial temperatures for G = 160 kg/(m^2.s).

Boiling curves for the cases with G = 160 kg/m^2 and T_i~70°C are shown in Figure 5.6. The blue case shows the response of the tube when the heater is left on after the quench, and the red case shows the tube when the heater is turned off after the quench. Similar to the cases shown in Figure 5.5, the decreases in temperature and heat flux overlap, validating the independence of nucleate boiling heat transfer mechanisms in response to different cooling conditions. This finding is important in that the unsteady flow boiling effects introduced by different cooling rates can be considered negligible when estimating heat transfer in the nucleate boiling regime among these conditions. This assumption needs to be validated for different flow geometries, higher temperatures, and different flow regimes, however.

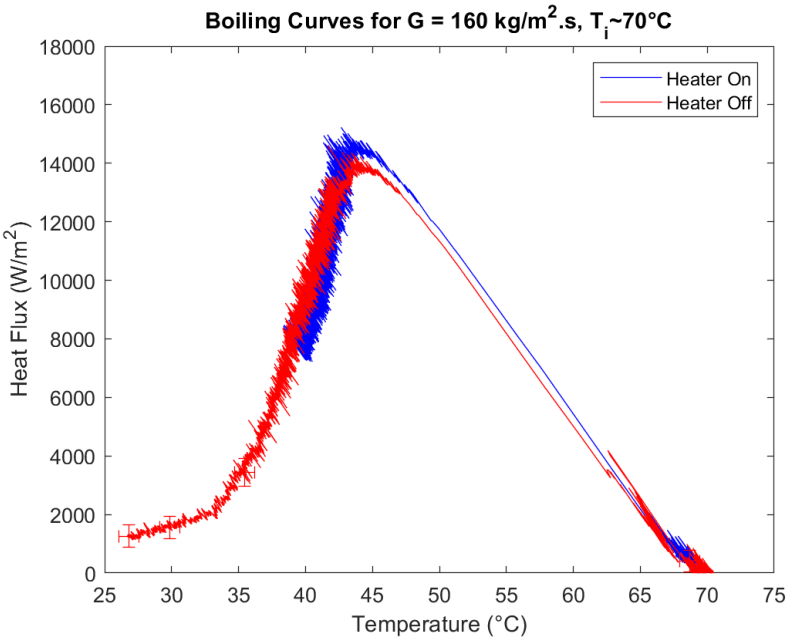

Figure 5.6: Quenching test boiling curves at different cooling conditions for G = 160 (kg/m^2.s).

5.3.2 Heat Transfer Coefficient

The average heat transfer coefficient after the quench at the center of the tube for each test at G = 80 kg/(m^2.s) is shown in Figure 5.7, alongside average heat transfer coefficient data from steady state heated tube tests described in Chapter 3. Figure 5.8 shows the heat transfer coefficient for the same conditions at the end of each quenching test. The test sections used for the quenching tests and the steady state tests were different, resulting in a difference in test section nucleation site density, which may explain the small disparity between the quenching data and the heated tube tests. Both sets of heat transfer coefficient data increase with increasing heat flux, and quenching tests where the heater was turned off show lower heat transfer after the quench than tests with the heater remained on. Correlations used by Hartwig et al. [20] and Mercado et al. [41], models from Kim & Mudawar [42] (equations 32-34) and Ogata & Sato [43] (equation 35) are also plotted in

Figures 5.7 and 5.8. Both the Kim & Mudawar and Ogata & Sato correlations are derived using the Dittus-Boelter correlation, which defines the heat transfer of a single-phase turbulent flow through a straight tube [23]. Kim & Mudawar expanded the Dittus-Boelter correlation by incorporating the effects of boiling dominant heat transfer h_b and convective boiling dominant heat transfer h_{cb}. They developed their correlation using 10,805 data points from 37 sources. Ogata & Sato acquired liquid helium flow boiling data and modified the Dittus-Boelter equation to incorporate boiling effects and two-phase turbulence. The Martinelli Parameter shown in equation 36 is used for both correlations.

$$h_{NB} = \sqrt{h_{bo}^2 + h_{cb}^2} \tag{32}$$

$$h_{bo} = \left[2345\left(Bo\frac{p_H}{p_w}\right)^{0.70}\left(\frac{P}{P_C}\right)^{0.38}(1-x)^{-0.51}\right]\left(0.023Re^{0.8}Pr^{0.4}\frac{k}{D_i}\right) \tag{33}$$

$$h_{cb} = \left[5.2\left(Bo\frac{p_H}{p_w}\right)^{0.08}We^{-0.54} + 3.5\left(\frac{1}{X_{tt}}\right)^{0.94}\left(\frac{\rho_v}{\rho_l}\right)^{0.25}\right]\left(0.023Re^{0.8}Pr^{0.4}\frac{k}{D_i}\right) \tag{34}$$

$$h_{NB} = (X_{tt}^{-0.66} + 1500Bo^{0.8})\left(0.015Re^{0.8}Pr^{0.4}\frac{k}{d}\right) \tag{35}$$

$$X_{tt} = \left(\frac{1-x}{x}\right)^{0.9}\left(\frac{\rho_v}{\rho_l}\right)^{0.5}\left(\frac{\mu_l}{\mu_v}\right)^{0.1} \tag{36}$$

The correlation by Kim & Mudawar [42] was developed for a variety of room temperature engineering fluids, and is applicable for inner diameters from 0.19-6.5 mm, qualities between 0-1, and mass fluxes between 19-1608 kg/(m^2.s). Ogata & Sato [43] developed their correlation using steady state liquid helium data through a tube with inner diameter 1.09 mm.

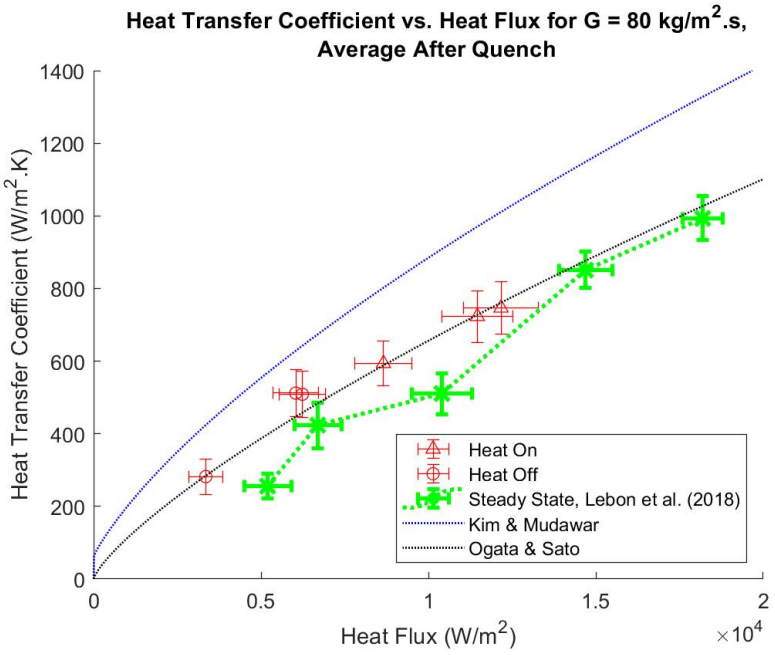

Figure 5.7: Average heat transfer coefficient at the center of the tube after the quench, steady state heated tube data, and correlations Kim & Mudawar and Ogata & Sato for G = 80 kg/(m^2.s).

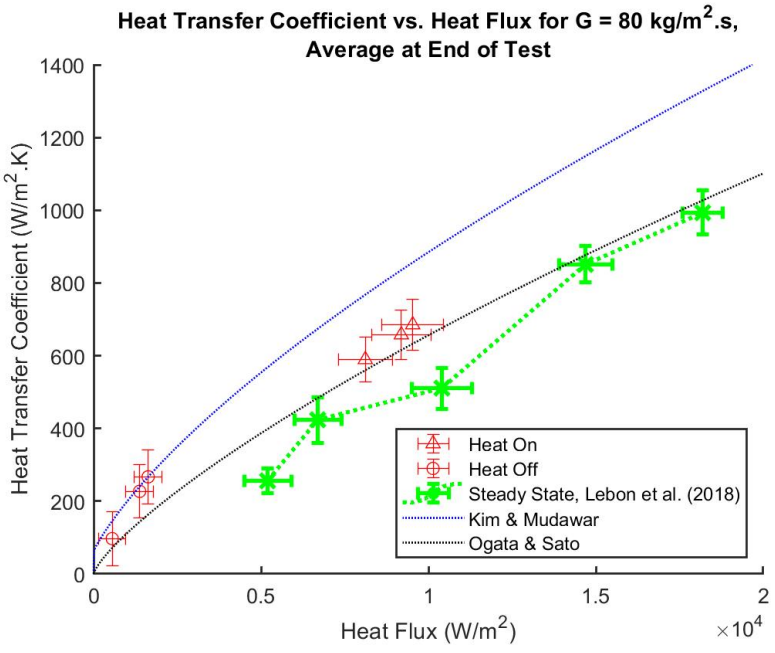

Figure 5.8: Average heat transfer coefficient at the center of the tube at the end of the quenching test, steady state heated tube data, and correlations Kim & Mudawar and Ogata & Sato for G = 80 kg/(m^2.s).

The Kim & Mudawar correlation overpredicts the nucleate boiling quenching data by 26% in the worst case, while the Ogata & Sato correlation underpredicts by 14% at worst. Hartwig et al. [40] found that Kim & Mudawar overpredicts cryogen quenching data by 189%-9887%, while Ogata & Sato overpredicts by 74%-6710%. The reason the quenching data with HFE-7000 in the sapphire tube are more consistent with correlations may be because the flow rapidly reaches pseudo-steady state boiling behavior for each case. The heat transfer coefficient data for each quench test are consistent for each heat flux and flow rate regardless of the time rate of change in wall temperature $\frac{dT_{wall}}{dt}$. Figure 5.9 shows a comparison of average heat transfer coefficients after the quench plotted as a function of the average wall temperature rate of change. The deviation observed in the heat transfer coefficient data are within the error margins for each separate heating condition and mass flux. The heat transfer coefficients for tests when the heater was turned off are lower since the flow is transitioning from nucleate boiling to single-phase heat transfer. This indicates the heat transfer coefficient using the sapphire tube test section and HFE-7000 is solely dependent on the local wall heat flux and mass flux. This may not be the case for cryogenic fluids, since transient effects may still be present

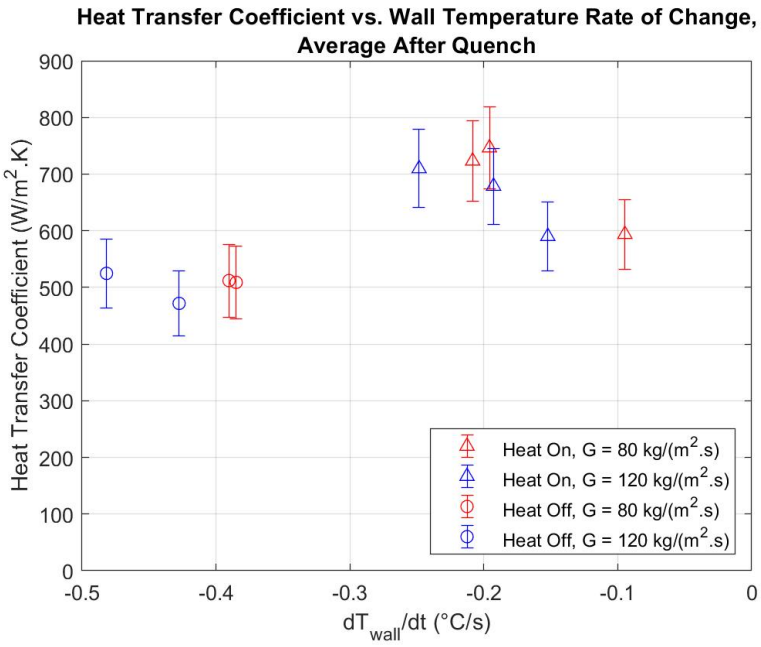

Figure 5.9: Average heat transfer coefficient at the center of the tube after the quench plotted vs. time rate of change in wall temperature.

To understand the differences between cryogen quenching studies and quenching of HFE-7000, non-dimensional parameters were computed to identify the key properties that are affecting the heat transfer. Table 5.1 lists non-dimensional parameters for the current work with HFE-7000 at a mass flow rate of 0.0023 kg/s (G = 80 kg/(m^2.s)), a tube inner diameter of 6 mm, and a saturation temperature of 34°C compared to liquid nitrogen experiments performed in Hartwig et al. [44] with a mass flow rate of 0.0044 kg/s, a tube inner diameter of 8 mm, and a saturation temperature of 79 K.

Table 5.1: Non-dimensional parameters of room temperature engineering fluid and cryogen quenching tests.

Non-dimensional parameter	**HFE-7000**	**LN_2 (Hartwig et al. [44])**
Reynolds number (Re)	1071	4319
Weber number (We)	2.21	8.64
Jakob number (Ja)	0.38	2.06
Prandtl number (Pr)	7.77	2.47
Density ratio (ρ_l/ρ_v)	179.9	179.1
Viscosity ratio (μ_l/μ_v)	29.94	37.33

The Jakob number for the cryogen quenching test is an order of magnitude larger than for the current study. A much larger wall superheat is present for cryogen chilldown tests since the boiling point is so much lower than the ambient. In the current study, the tube is heated to a desired superheat before quenching, but much higher temperatures are necessary to capture the transient effects involved in film and transition boiling. Reynolds and Weber numbers are both lower for the tests with HFE-7000. These parameters can be matched by increasing the test section flow rate. To simulate liquid nitrogen quenching using room temperature fluids, mass flux and wall superheat must be increased significantly. The current test configuration is limited to a mass flux of 240 kg/(m^2.s), which corresponds to a Reynolds number of 3214. A more powerful pump, a larger tube diameter, or a working fluid with lower viscosity is required to reach Reynolds numbers observed in the literature. The Prandtl number, density ratio and viscosity ratio cannot be adjusted, since they are directly dependent on fluid properties.

5.4 SUMMARY OF CONTRIBUTIONS

A method of generating vapor within a heated tube by incorporating a bypass valve was implemented. Quenching data in the nucleate boiling regime were acquired for HFE-7000 flowing through a 6 mm ID tube for various flow rates and initial temperatures. Each test condition was recorded both leaving the test section heater on and turning it off, simulating different cooling conditions. Boiling curves were generated for tests for each initial temperature and heating condition. The overlapping boiling curves indicate nucleate boiling during quenching with HFE-7000 can be considered quasi-steady for the initial temperatures between 50-75°C. Heat transfer coefficient data were found to be within 26% of correlative estimations used by Kim & Mudawar [42] and Ogata & Sato [43]. These correlations have an error of 74-9887% when predicting quenching heat transfer coefficient for cryogens. The reasons for this large disparity are that cryogen tests may not be considered quasi-steady, and correlations are typically developed using room temperature engineering fluids. A scaling analysis shows that mass flux and initial temperature must increase significantly for experiments using engineering fluids to properly simulate cryogen studies. Future studies using this quenching setup must also reach higher temperatures to study film boiling and transition boiling.

CHAPTER 6: CONCLUSION

Flow boiling heat transfer behavior at varying gravity levels using a local temperature measurement technique has been investigated. The effects of convective motion and evaporation on the heat transfer could be seen locally along the tube wall. For the nine gravity levels tested, transition regimes were observed at different flow and heating conditions. In microgravity, there was a noticeable reduction in bubbly flow heat transfer compared to terrestrial gravity due to the decrease in slip velocity, bubble detachment frequency, and turbulent mixing. The reduction in heat transfer was continuous across all gravity levels only if the flow regime was consistently bubbly flow. In certain cases, single phase flow was observed in terrestrial gravity while two phase flow was observed in microgravity. The rapid growth of the thermal boundary layer in microgravity for these cases promoted nucleation, resulting in higher heat transfer coefficients compared to terrestrial flow. The effect of gravity on heat transfer decreased as both mass flux and heat flux increased. At high mass flux, the forced convection dominated the gravity effect. At high heat flux, the annular flow liquid film evaporation dominated the gravity effect. Churn flow and mixed regimes were observed in downward flow due to the opposing effects of buoyancy and inertial forces, while mostly bubbly flow was observed in microgravity and upward flow. Knowledge of the flow regime boundaries was demonstrated to be important in predicting reduced-gravity flow boiling heat transfer.

It is feasible to predict microgravity isolated bubbly flow boiling heat transfer using single-phase heat transfer models if the local axial velocity is used. Microgravity bubbly flow boiling heat transfer could be predicted using single-phase laminar modeling and the local liquid velocity if the liquid remains laminar (low liquid Reynolds numbers and no

bubble coalescence). The dominant heat transfer mechanism in these cases was laminar forced convection since there was little wake mixing around the bubbles. The coalescence mechanism needs to be well understood to model flow under these conditions. Models incorporating a negligible slip velocity and an accelerating liquid velocity profile are proposed.

Quenching heat transfer was studied to determine the efficacy of flow boiling heat transfer models in the nucleate boiling regime during chilldown. The comparison of experimental data with applicable heat transfer correlations showed significantly less error when testing room temperature engineering fluids compared to cryogenic fluids in the literature. The accuracy of correlations for cryogens improves for steady state heated tests as opposed to quenching tests, meaning currently available correlative estimations may not be feasible for the inherently transient process of chilldown. Heat transfer coefficient data for HFE-7000 was deemed pseudo-steady state for the initial temperatures and flow rates tested. It has been determined that future studies involving the quenching of room temperature engineering fluids must work to match non-dimensional parameters when comparing correlative estimations.

6.1 FUTURE STUDIES AND RECOMMENDATIONS

Additional local flow boiling data must be taken for the prescribed conditions at saturation for microgravity, lunar gravity, Martian gravity, terrestrial gravity, and hyper gravity for upward and downward flow. These could be used to verify the potential of the proposed bubbly, slug, and annular flow microgravity models. The homogeneous bubbly flow model could be verified using the saturated data at low heat flux. Microchannel flow boiling analogues for microgravity slug flow could also be evaluated. Due to the short test section

length and therefore the insufficient development length for typical slug flow, a finer range of heat fluxes must be studied in order to appropriately capture microgravity slug flow conditions. Derivation of annular flow film thickness and liquid velocity profile could be used to verify annular flow heat transfer models in microgravity. Finally, transition criteria of gravity-dominated heat transfer within each regime must be analyzed using additional partial and hyper gravity data. There is a significant dearth of partial gravity results due to the limited opportunities for testing in those conditions. The results of additional local saturated flow boiling data at various gravity levels will highlight the importance of studying separate flow boiling regimes and the influence of gravity on each.

Quenching data must be taken in broader test conditions in order to match non-dimensional parameters observed in cryogenic conditions. Higher temperatures will have to be tested to completely characterize both film and transition boiling. Holistic analysis for film, transition, and nucleate boiling must be performed for to understand the transient effects of the full chilldown process before microgravity chilldown experiments can commence. Microgravity chilldown experiments using local TSP methods could provide valuable insight in modeling efforts for cryogen transfer in space, thus optimizing chilldown times and wasted cryogen.

APPENDIX A: UNCERTAINTY

A.1 MINIMIZING HEAT TRANSFER COEFFICIENT UNCERTAINTY

The uncertainty in the heat transfer coefficient can be found by applying the following error propagation equation to the calculated heat transfer coefficient:

$$\delta h = \sqrt{\sum_{i=1}^{n} \left(\frac{\partial h}{\partial x_i} \delta x_i \right)^2} \tag{37}$$

Where n is the number of variables, and x_i are the variables within the equation $h = h(x_1,x_2,\ldots,x_n)$. The equation for the heat transfer coefficient h can be found by combining the conduction heat transfer across the adhesive insulator and the convection heat transfer into the bulk fluid, shown schematically in Figure A.1. Here, T_b, T_w, and T_s are the bulk, wall, and sapphire temperatures, respectively. The adhesive has thermal conductivity k_a and thickness t_a. This equation assumes that axial conduction out of the ends of the adhesive insulator layer is negligible.

$$\dot{q}''_{conduction} = k_a \frac{T_s - T_w}{t_a} \tag{38}$$

$$\dot{q}''_{convection} = h(T_w - T_b) \tag{39}$$

$$\dot{q}''_{conduction} = \dot{q}''_{convection} = \dot{q}'' \tag{40}$$

$$h = \frac{k_a}{t_a} \frac{T_s - T_w}{T_w - T_b} \tag{41}$$

$$h = \frac{k_a}{t_a} \frac{\Delta T_{sw}}{\Delta T_{wb}} \tag{42}$$

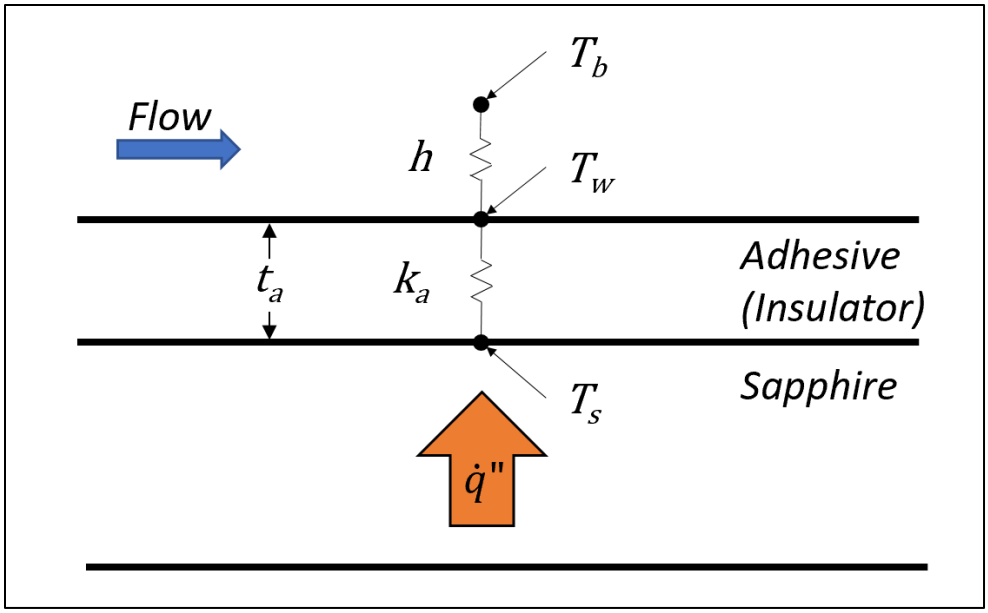

Figure A.1: Schematic diagram of TSP stack used for heat transfer equations

Applying the error propagation equation to the heat transfer equation results in the following:

$$\delta h = \sqrt{\left(\frac{\partial h}{\partial k_a}\delta k_a\right)^2 + \left(\frac{\partial h}{\partial t_a}\delta t_a\right)^2 + \left(\frac{\partial h}{\partial \Delta T_{sw}}\delta \Delta T_{sw}\right)^2 + \left(\frac{\partial h}{\partial \Delta T_{wb}}\delta \Delta T_{wb}\right)^2} \tag{43}$$

$$\delta h = \sqrt{\left(\frac{1}{t_a}\frac{\Delta T_{sw}}{\Delta T_{wb}}\delta k_a\right)^2 + \left(\frac{-k_a}{t_a^2}\frac{\Delta T_{sw}}{\Delta T_{wb}}\delta t_a\right)^2 + \left(\frac{k_a}{t_a}\frac{1}{\Delta T_{wb}}\delta \Delta T_{sw}\right)^2 + \left(\frac{-k_a}{t_a}\frac{\Delta T_{sw}}{\Delta T_{sw}^2}\delta \Delta T_{wb}\right)^2} \tag{44}$$

A normalized version of the equation is shown below:

$$\frac{\delta h}{h} = \sqrt{\left(\frac{\delta k_a}{k_a}\right)^2 + \left(\frac{-\delta t_a}{t_a}\right)^2 + \left(\frac{\delta \Delta T_{sw}}{\Delta T_{sw}}\right)^2 + \left(\frac{-\delta \Delta T_{wb}}{\Delta T_{wb}}\right)^2} \tag{45}$$

This equation has several variables that are beyond experimental control, including k_a, δk_a, δt_a, $\delta \Delta T_{sw}$, and $\delta \Delta T_{wb}$. The uncertainty is therefore minimized when t_a, ΔT_{sw}, and ΔT_{wb} are maximized. While t_a is a variable that we can directly control during the TSP stacking process, ΔT_{sw} and ΔT_{wb} are affected by varying test parameters. However, it is known that ΔT_{sw} increases as t_a increases and ΔT_{wb} increases as h decreases. It is therefore required to

find an ideal thickness t_a which can provide low uncertainty under various testing conditions. This can be identified by setting the temperature differentials to be equal, resulting in the following criterion:

$$t_a = \frac{k_a}{h} \tag{46}$$

The limitations on these variables include physical and thermal restrictions. It is anticipated that a maximum temperature of 100°C is the most valuable restriction, while a heat transfer coefficient range of 200-2000 W/(m^2·K) will cover most testing parameters. We can find the ideal thicknesses for this range using a bulk temperature of 34°C, and an adhesive thermal conductivity of 0.2 W/(m.K).

$$\underline{\text{For h = 200 W/m}^2\text{K:}}\ t_a = \frac{k_a}{h} = \frac{0.2\frac{W}{mK}}{200\frac{W}{m^2K}} = 0.001\ m \tag{47}$$

$$\underline{\text{For h = 2000 W/m}^2\text{K:}}\ t_a = \frac{k_a}{h} = \frac{0.2\frac{W}{mK}}{2000\frac{W}{m^2K}} = 0.0001\ m \tag{48}$$

If an approximate midpoint of 0.0005 m for the thickness of the adhesive insulator is used, the temperature differences at each heat transfer coefficient can be calculated. First, a maximum temperature of 100°C is imposed to check the temperature differences irrespective of heat flux.

$\underline{\text{For h = 200 W/m}^2\text{k, t}_a\text{ = 0.0005 m, T}_s\text{ = 100°C}}$

$$h = \frac{k_a}{t_a}\frac{T_s - T_w}{T_w - T_b},\ T_w = \frac{\frac{ht_a}{k_a}T_b + T_s}{\frac{ht_a}{k_a}+1} = \frac{\frac{200\frac{W}{m^2K}0.0005m}{0.2\frac{W}{mK}}34°C + 100°C}{\frac{200\frac{W}{m^2K}0.0005m}{0.2\frac{W}{mK}}+1} = 78°C \tag{49}$$

$$\Delta T_{wb} = 44°C, \Delta T_{sw} = 22°C$$

For h = 2000 W/m^{2}k, t_a = 0.0005 m, T_s = 100°C

$$h = \frac{k_a}{t_a}\frac{T_s - T_w}{T_w - T_b},\ T_w = \frac{\frac{ht_a}{k_a}T_b + T_s}{\frac{ht_a}{k_a}+1} = \frac{\frac{2000\frac{W}{m^2K}0.0005m}{0.2\frac{W}{mK}}34°C + 100°C}{\frac{2000\frac{W}{m^2K}0.0005m}{0.2\frac{W}{mK}}+1} = 45°C \quad (50)$$

$$\Delta T_{wb} = 9°C, \Delta T_{sw} = 55°C$$

Next, a heat flux of 10,000 W/m^2 is imposed at heat transfer coefficients of 200-2000 W/(m^2.K) to check if the maximum temperature is below 100°C and if the temperature differences are greater than the temperature uncertainty.

For h = 200 W/m^{2}K, t_a = 0.0005 m, q" = 10,000 W/m^2

$$\dot{q}" = h(T_w - T_b),\ T_w = \frac{\dot{q}"}{h} + T_b = \frac{10{,}000\frac{W}{m^2}}{200\frac{W}{m^2K}} + 34°C = 84°C \quad (51)$$

$$\dot{q}" = k\frac{T_s - T_w}{t_a},\ T_s = \frac{\dot{q}"t_a}{k} + T_b = \frac{10{,}000\frac{W}{m^2}*0.0005m}{0.2\frac{W}{mK}} + 84°C = 109°C \quad (52)$$

For h = 2000 W/m^{2}K, t_a = 0.0005 m, q" = 10,000 W/m^2 (53)

$$\dot{q}" = h(T_w - T_b),\ T_w = \frac{\dot{q}"}{h} + T_b = \frac{10{,}000\frac{W}{m^2}}{2000\frac{W}{m^2K}} + 34°C = 39°C$$

$$\dot{q}" = k\frac{T_s - T_w}{t_a},\ T_s = \frac{\dot{q}"t_a}{k} + T_b = \frac{10{,}000\frac{W}{m^2}*0.0005m}{0.2\frac{W}{mK}} + 39°C = 64°C \quad (54)$$

In all cases tested, the minimum temperature difference is 5°C. This is due to the high heat transfer coefficient of 2000 (W/m^2.K) forcing a very small temperature difference between the wall and bulk fluid. The maximum temperature amongst all cases tested is 109°C. This could be mitigated by decreasing the thickness to 0.00032 m. Increasing the thickness to several hundred microns will significantly decrease the uncertainty in *h*. Using the parameters from the worst-case scenario, a heat transfer coefficient uncertainty of 20% is

seen (shown below). This can be reduced to as low as 7% at lower imposed heat transfer coefficients.

Table A.1: Values and uncertainties of test section parameters used in heat transfer coefficient calculation.

Variable	**X_i**	**δX_i**	**Units**
k_a	0.2	0.01	W/m.K
t_a	0.0005	1e-6	m
ΔT_{sw}	25	0.9899	°C
ΔT_{wb}	5	0.9899	°C

$$\frac{\delta h}{h} = \sqrt{\left(\frac{\delta k_a}{k_a}\right)^2 + \left(\frac{-\delta t_a}{t_a}\right)^2 + \left(\frac{\delta \Delta T_{sw}}{\Delta T_{sw}}\right)^2 + \left(\frac{-\delta \Delta T_{wb}}{\Delta T_{wb}}\right)^2} \tag{55}$$

$$\frac{\delta h}{h} = \sqrt{\left(\frac{0.01}{0.2}\right)^2 + \left(\frac{-0.000001}{0.0005}\right)^2 + \left(\frac{0.9899}{25}\right)^2 + \left(\frac{-0.9899}{5}\right)^2} \tag{56}$$

$$\frac{\delta h}{h} = \sqrt{0.0025 + 0.000004 + 0.0016 + 0.0392} \tag{57}$$

APPENDIX B: PROPERTY MEASUREMENT

B.1 THERMAL CONDUCTIVITY OF PET FILM

The thermal conductivity (k) of a PET film sample was measured. The measurement procedure involved two copper plates, two thermocouples, a FluxTeq heat flux sensor, a Minco film heater, and a chiller. The test setup is shown schematically in Figure B.1 below.

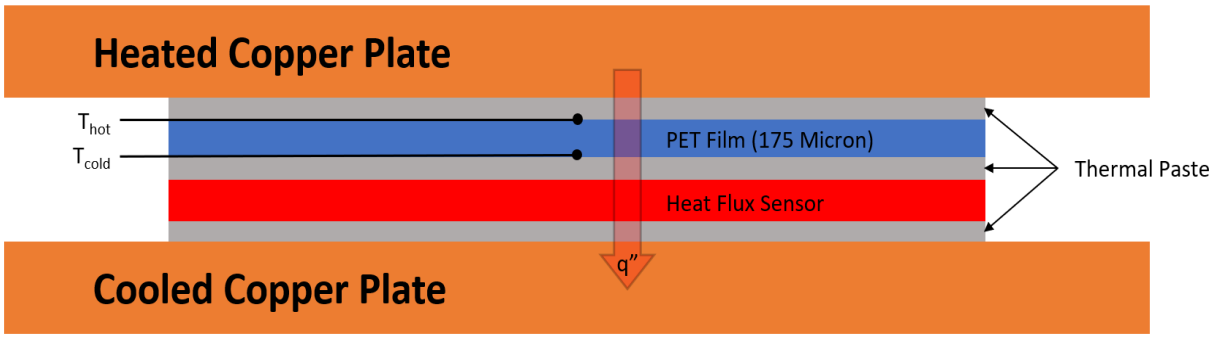

Figure B.1: Thermal conductivity test setup (not to scale).

A 175 μm thick PET film was cut to the shape of the heat flux sensor. The PET film was placed on top of the heat flux sensor and then pressed between both copper plates with thermal paste in between each layer. The thermocouples were placed on either end of the PET film to measure the temperature difference across the sample (T_{hot} and T_{cold}). The Minco film heater was adhered to the top of one copper plate (heated copper plate), and 115 V wall power was supplied to the heater. A copper tube was soldered onto the end of the other copper plate (cooled copper plate), and chilled water at 12°C was circulated through the tube. The layered setup was pressed together between the heated and cooled copper plates by tightening screws connecting the plates. A gasket was placed between the plates around the PET sample to prevent heat leaking in the transverse direction. The

thermocouple temperatures were recorded using a National Instruments thermocouple DAQ and National Instruments Labview. The heat flux sensor was calibrated by Fluxteq, and its measurements were recorded using a Fluxteq DAQ. 50 temperature and heat flux measurements were recorded and averaged. The heat flux reached steady state before measurements were taken (Figure B.2).

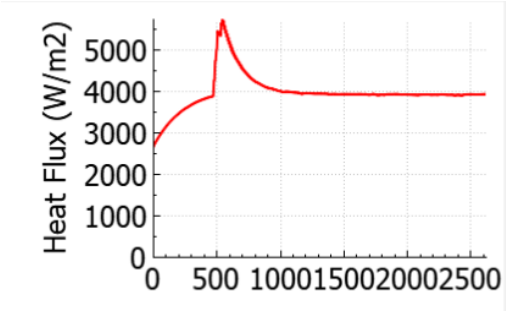

Figure B.2: Measured heat flux vs. time (s) during entire session. Measurements were recorded at the end of the session.

The average hot temperature, cold temperature, and heat flux were implemented in Fourier's law to calculate the thermal conductivity of the PET sample. A measured thickness (t_{PET}) of 175 microns was used for the PET sample's thickness. These values and the resulting k are shown in Table B.1.

$$\dot{q}'' = k\frac{dT}{dx} \tag{58}$$

$$\dot{q}'' = k\frac{T_{hot} - T_{cold}}{t_{PET}} \tag{59}$$

Table B.1: Measured values for thermal conductivity measurement and resulting thermal conductivity of PET film sample.

T_{hot} (°C)	T_{cold} (°C)	q" (W/m^2)	t_{PET} (μm)	k (W/m.K)
33.09	27.16	3939.5	175	0.116

The reported accuracies for both the heat flux sensor and thermocouples are 5%. The thickness measurement was performed using a micrometer with an accuracy of 1 μm. Propagating the error results in an equation for the uncertainty in thermal conductivity shown below:

$$\frac{\delta k}{k} = \sqrt{\left(\frac{\delta T_{hot}}{T_{hot}}\right)^2 + \left(\frac{\delta T_{cold}}{T_{cold}}\right)^2 + \left(\frac{\delta \dot{q}''}{\dot{q}''}\right)^2 + \left(\frac{\delta t_{PET}}{t_{PET}}\right)^2} \tag{60}$$

Substituting the values for the current test results in a thermal conductivity uncertainty of ±0.01 W/m.K.

REFERENCES

[1] J. McQuillen, E. Rame, M. Kassemi, B. Singh, B. Motil, (2003). Results of the Workshop on Two-Phase Flow, Fluid Stability and Dynamics: Issues in Power, Propulsion, and Advanced Life Support Systems, NASA/TM-2003-212598.

[2] F.P. Chiaramonte, J.A. Joshi, (2004) Workshop on Critical Issues in Microgravity Fluids, Transport, and Reaction Processes in Advanced Human Support Technology", NASA/TM—2004-212940.

[3] "Microgravity Research in Support of Technologies for the Human Exploration and Development of Space and Planetary Bodies", Committee on Microgravity Research, National Academy Press, 2000.

[4] "Review of NASA Plans for the International Space Station" National Academy Press, 2006.

[5] H. Ohta, Experiments on microgravity boiling heat transfer by using transparent heaters, Nuclear Engineering and Design 175(1) (1997) 167-180.

[6] C. Baltis, G.P. Celata, M. Cumo, L. Saraceno, G. Zummo, Gravity influence on heat transfer rate in flow boiling, Microgravity Science and Technology 24(3) (2012) 203-213.

[7] M. Narcy, E. De Malmazet, C. Colin, Flow boiling in tube under normal gravity and microgravity conditions, Int. J. of Multiphase Flow 60 (2014) 50-63, https://doi.org/10.1016/j.ijmultiphaseflow.2013.11.011.

[8] H. Zhang, I. Mudwar, M.M. Hasan, Experimental and Theoretical study of orientation effects on flow boiling CHF, Int J. of Heat and Mass Transfer 45 (2002) 4463-4477.

[9] H. Zhang, I. Mudwar, M.M. Hasan, Experimental assessment of the effects of body force, surface tension force, and inertia on flow boiling CHF, Int J. of Heat and Mass Transfer 45 (2002), 4479-4495.

[10] H. Zhang, I. Mudwar, M.M. Hasan, Flow boiling CHF in microgravity. Int. J. of Heat and Mass Transfer 48(15) (2005), 3107-3118.

[11] T.H. Kim, E. Kommer, S. Dessiatoun, J. Kim, Measurement of two-phase flow and heat transfer parameters using infrared thermometry, Int. J. of Multiphase Flow 40 (2012) 56-67.

[12] B.T. Campbell, T. Liu, J.P. Sullivan, Temperature Sensitive Fluorescent Paint Systems, in: Proc. 18th AIAA Aerospace Ground Testing Conference, Colorado Spring, CO, 1994.

[13] H. Ozawa, S.J. Laurence, J. Martinez Schramm, A. Wagner, K. Hannemann, Fast-response temperature-sensitive-paint measurements on a hypersonic transition cone, Experiments in Fluids 56(1853) (2015) 2-13.

[14] M. Kim, M. Yoda, 2010, Fluorescence Thermometry for Measuring Wall Surface and Bulk Fluid Temperatures, 2010 14th International Heat Transfer Conference, Washington, DC, Paper no. IHTC14-22884.

[15] A. Shibuya, R. Ueki, Y. Suzuki, M. Tange, Temporal temperature distribution measurement of a heat transfer surface of a flow boiling heat sink with a micro-gap using temperature sensitive paint, Proceedings of the First Pacific Rim Thermal Engineering Conference, Hawaii, 2016 Paper no. PRTEC-14900.

[16] H. Al Hashimi, C.F. Hammer, M.T. Lebon, D. Zhang, J. Kim, Phase-Change Heat Transfer Measurements Using Temperature-Sensitive Paints, ASME J. of Heat Transfer 140(3) (2018) 031601.
[17] R. Raj, J. Kim, J. McQuillen, Pool boiling heat transfer on the International Space Station: Experimental results and model verification, ASME J. of Heat Transfer 134(10) (2012) 101504, DOI: 10.1115/1.4004370.
[18] M. Lebon, C. Hammer, J. Kim, Gravity effects on subcooled flow boiling heat transfer, Int. J. of Heat and Mass Transfer 128 (2019) 700-714, DOI: 10.1016/j.ijheatmasstransfer.2018.09.011.
[19] M.T. Lebon, C.F. Hammer, J. Kim, Using a modified single-phase model to predict microgravity flow boiling heat transfer in the bubbly flow regime, Exp. Heat Transfer (2020), DOI: 10.1080/08916152.2020.1782534.
[20] J. Hartwig, S. Darr, and A. Asencio, Assessment of existing two phase heat transfer coefficient and critical heat flux correlations for cryogenic flow boiling in pipe quenching experiments, Int. J. of Heat and Mass Transfer 93 (2016) 441-463.
[21] M.H. Rausch, L. Kretschmer, S. Will, A. Leipertz, A.P. Fröba, Density, Surface Tension, and Kinematic Viscosity of Hydrofluoroethers HFE-7000, HFE-7100, HFE-7200, HFE-7300, and HFE-7500, J. Chem. Eng. Data 60 (2015), DOI: 10.1021/acs.jced.5b00691.
[22] M. Lebon. Etude de la dynamique de bulles formées en paroi par injection ou ébullition: effet de la gravité et des forces hydrodynamiques (Doctoral dissertation), University of Toulouse, (2016), oatao.univ-toulouse.fr.
[23] F.P. Incropera, D.P. DeWitt, T.L. Bergman, A.S. Lavine, 2007, Fundamentals of Heat and Mass Transfer, Wiley, Hoboken, NJ.
[24] L.P. Davis, J.J. Perona, Development of free convection flow of a gas in a heated vertical open tube, Int. J. of Heat and Mass Transfer 14(7) (1971) 889-903.
[25] R.K. Shah, A.L. London, Laminar flow forced convection in ducts a sourcebook for compact heat transfer exchange analytical data. Elsevier, Amsterdam, the Netherlands 1978.
[26] K. Stephan, Warmeubergang bei turbulenter und bei laminarer Stromung in Ringspalten, Chem.-Ing.-Tech. 34(3) (1962) 207-212.
[27] C. Colin, J. Fabre, J. McQuillen, Bubble and slug flow at microgravity conditions: state of knowledge and open questions, Chemical Engineering Communications 141(1) (1996) 155-173.
[28] A. Scammell, J. Kim, Heat transfer and flow characteristics of rising Taylor bubbles, Int. J. of Heat and Mass Transfer 89 (2015) 379-389.
[29] V. P. Carey, Liquid-Vapor Phase-Change Phenomena: An Introduction to the Thermophysics of Vaporization and Condensation Processes in Heat Transfer Equipment. Washington, D.C.: Hemisphere Pub. Corp., 1992.
[30] T. Takamasa, K. Kondo, M. Kawase, K. Rezkallah, and N. Clarke, Measurement of interfacial configuration of bubbly flow under normal and microgravity conditions using stereo image-processing method, in Trans JSME B 63(606) (1997) 396-403.
[31] J. McQuillen, C. Colin, and J. Fabre, Ground-based gas–liquid flow research in microgravity conditions: state of knowledge, Space Forum 3, pp. 165-457, 1998.

[32] C. Colin, O. Kannengieser, W. Bergez, M. Lebon, J. Sebilleau, M. Sagan, and S. Tanguy, Nucleate pool boiling in microgravity: recent progress and future prospects, C. R. Mécanique 345(1) (2017) 21-34, DOI: 10.1016/j.crme.2016.10.004.
[33] M. Ishii, One-dimensional drift-flux model and constitutive equations for relative motion between phases in various two-phase flow regimes, Argonne Nat. Lab., Lemont, IL, ANL-77-47, 1977. DOI: 10.2171/6871478.
[34] T. Hibiki and M. Ishii, Distribution parameter and drift velocity of drift–flux model in bubbly flow, Int. J. of Heat Mass Transfer 45(4) (2002) 707-721, DOI: 10.1016/S0017-9310(01)00195-8.
[35] T. Hibiki, T. Takamasa, and M. Ishii, One-dimensional drift-flux model and constitutive equations for relative motion between phases in various two-phase flow regimes at microgravity conditions, in 12th Int. Conference on Nuclear Engineering Proc. (2004) 377-386.
[36] W.N. Bond and D.A. Newton, LXXXII. Bubbles, drops, and Stokes' law (Paper 2), The London, Edinburgh, and Dublin Philosophical Magazine and J. of Sci. 5(30) (1928) 794-800, DOI: 10.1080/14786440408564523.
[37] G.B. Wallis, The terminal speed of single drops or bubbles in an infinite medium, Int. J. of Multiph. Flow 1(4) (1974) 491-511, DOI: 10.1016/0301-9322(74)90003-2.
[38] W.M. Kays, M.E. Crawford, and B. Weigand, Convective Heat and Mass Transfer. New York, NY: McGraw-Hill, 2005.
[39] G.B. Wallis, One-Dimensional Two-Phase Flow. New York: John Wiley, 1965.
[40] S. Darr, J. Dong, N. Glikin, J. Hartwig, A. Majumdar, A. Leclair and J. Chung, The effect of reduced gravity on cryogenic nitrogen boiling and pipe chilldown, Nature Partner Journals Microgravity 2(16033) (2016).
[41] M. Mercado, N. Wong and J. Hartwig, Assessment of two-phase heat transfer coefficient and critical heat flux correlations for cryogenic flow boiling in pipe heating experiments, Int. J. of Heat and Mass Transfer 133 (2019) 295 -315.
[42] S. Kim, I. Mudawar, Review of databases and predictive methods for heat transfer in condensing and boiling mini/micro-channel flows, Int. J. of Heat and Mass Transfer 77 (2014) 627-652.
[43] H. Ogata, S. Sato, Forced convection heat transfer to boiling helium in a tube, Cryogenics 14(7) (1974) 375-380.
[44] J. Hartwig, H. Hu, J. Styborski, J.N. Chung, Comparison of cryogenic flow boiling in liquid nitrogen and liquid hydrogen chilldown experiments, Int. J. of Heat and Mass Transfer 88 (2015) 662-673.